



Carbon and nitrogen flows during a bloom of the coccolithophore *Emiliana huxleyi*: Modelling a mesocosm experiment

P. Joassin^{a,*}, B. Delille^b, K. Soetaert^c, J. Harlay^{b,d}, A.V. Borges^b, L. Chou^d, U. Riebesell^e, K. Suykens^b, M. Grégoire^a

^a Oceanology Laboratory, Interfaculty Centre for Marine Research, Université de Liège, Institut de Chimie (B6c), B-4000 Liège, Belgium

^b Unité d'Océanographie Chimique, Interfaculty Centre for Marine Research, Université de Liège, Institut de Physique (B5), B-4000 Liège, Belgium

^c Centre for Estuarine and Marine Ecology, Netherlands Institute of Ecology, Yerseke, The Netherlands

^d Laboratoire d'Océanographie Chimique et Géochimie des Eaux, Université Libre de Bruxelles, Campus de la Plaine, Brussels, Belgium

^e Leibniz Institute of Marine Sciences, IFM-GEOMAR, Kiel, Germany

ARTICLE INFO

Article history:

Received 24 June 2010

Received in revised form 26 November 2010

Accepted 30 November 2010

Available online 10 December 2010

Keywords:

Coccolithophore

Emiliana huxleyi

Mathematical model

Biogeochemical cycling

Calcification

Mesocosm experiment

ABSTRACT

A dynamic model has been developed to represent biogeochemical variables and processes observed during experimental blooms of the coccolithophore *Emiliana huxleyi* induced in mesocosms over a period of 23 days. The model describes carbon (C), nitrogen (N), and phosphorus (P) cycling through *E. huxleyi* and the microbial loop, and computes pH and the partial pressure of carbon dioxide ($p\text{CO}_2$) from dissolved inorganic carbon (DIC) and total alkalinity (TA). The main innovations are: 1) the representation of *E. huxleyi* dynamics using an unbalanced growth model in carbon and nitrogen, 2) the gathering of formulations describing typical processes involved in the export of carbon such as primary production, calcification, cellular dissolved organic carbon (DOC) excretion, transparent exopolymer (TEP) formation and viral lyses, and 3) an original and validated representation of the calcification process as a function of the net primary production with a modulation by the intra-cellular N:C ratio mimicking the effect of nutrients limitation on the onset of calcification. It is shown that this new mathematical formulation of calcification provides a better representation of the dynamics of TA, DIC and calcification rates derived from experimental data compared to classically used formulations (e.g. function of biomass or of net primary production without any modulation term).

In a first step, the model has been applied to the simulations of present $p\text{CO}_2$ conditions. It adequately reproduces the observations for chemical and biological variables and provides an overall view of carbon and nitrogen dynamics. Carbon and nitrogen budgets are derived from the model for the different phases of the bloom, highlighting three distinct phases, reflecting the evolution of the cellular C:N ratio and the interaction between hosts and viruses. During the first phase, inorganic nutrients are massively consumed by *E. huxleyi* increasing its biomass. Uptakes of carbon and nitrogen are maintained at a constant ratio. The second phase is triggered by the exhaustion of phosphate (PO_4^{3-}). Uptake of carbon and nitrogen being uncoupled, the cellular C:N ratio of *E. huxleyi* increases. This stimulates the active release of DOC, acting as precursors for TEP. The third phase is characterised by an enhancement of the phytoplankton mortality due to viral lysis. A huge amount of DOC has been accumulated in the mesocosm.

© 2010 Elsevier B.V. All rights reserved.

1. Introduction

Past records reveal the presence of the coccolithophore *Emiliana huxleyi* for 270,000 years. During the last 70,000 years, it has become the most numerically important species of coccolithophores. It is abundant in most seas except for the Arctic and Antarctic oceans (Paasche, 2002). In addition to its worldwide distribution and its

presence through the ages, *E. huxleyi* populations are remarkable in their capacity to produce large blooms during which dissolved inorganic carbon (DIC) dynamics is affected by the fixation of carbon dioxide (CO_2) through primary production and the production of calcite (Paasche, 2002; Suykens et al., 2010; Harlay et al., 2011). Another typical characteristic of *E. huxleyi* is the production of transparent exopolymer particles (TEP), an organic substance rich in carbon, refractory to microbial degradation, that promotes aggregation (Passow, 2002). The convergence of these biological features makes *E. huxleyi* one of the major drivers of oceanic carbon export (Buitenhuis et al., 2001).

* Corresponding author.

E-mail address: Pascal.Joassin@student.ulg.ac.be (P. Joassin).

Several models proposed and tested formulations describing the biogeochemical processes characteristic of phytoplankton blooms (e.g. Aksnes et al., 1994; Tyrrell and Taylor, 1996; Buitenhuis et al., 1996; Van Den Meersche et al., 2004; Merico et al., 2004; Oguz and Merico, 2006; Schartau et al., 2007). Buitenhuis et al. (2001) represent calcification by *E. huxleyi* during nitrate + nitrite (NO_x^-) limited conditions to evaluate the DIC balance between photosynthesis and calcification. Van Den Meersche et al. (2004) describe carbon over-consumption, a typical feature in phytoplankton species, such as coccolithophores, under nutrient limited conditions (e.g. Toggweiler, 1993; Anderson and Sarmiento, 1994; Banse, 1994), and its impact on DIC dynamics. The cellular exudates resulting from carbon over-consumption may support chemical transformations, becoming the precursor of TEP (Engel et al., 2004a,b). Schartau et al. (2007) describe the different steps of the formation of TEP through the coagulation of acidic polysaccharides (PCHO) provided by the cellular exudates occurring in a mesocosm diatom bloom.

In the frame of larger biogeochemical scales, some models investigate the impact of coccolithophores in global ecological systems where other phytoplankton species are also represented. These models focus on factors triggering blooms and controlling their seasonal cycles (e.g. Aksnes et al., 1994; Tyrrell and Taylor, 1996; Merico et al., 2004; Oguz and Merico, 2006). They emphasize nitrogen cycling and the dynamics of coccolithophores is modelled using a carbon–nitrogen balanced growth model. For instance, in Merico et al. (2004) and Oguz and Merico (2006), the dynamics of *E. huxleyi* is represented by its nitrogen content. Therefore, these models of coccolithophores do not simulate the temporal decoupling between the uptake of carbon and nitrogen, although this decoupling has been observed in declining bloom conditions (Engel et al., 2005). Such an evolution of the models should be a pre-requisite for the representation of TEP dynamics via carbon over-consumption in order to better represent carbon export.

The model presented in this paper is developed to represent *E. huxleyi* blooms experimentally induced in a mesocosm experiment carried out in Bergen (Norway) in June 2001 (Engel et al., 2004a,b, 2005; Rochelle-Newall et al., 2004; Delille et al., 2005). The data set provided by this experiment (see Section 2.1 for details) allows testing and validating explicit formulations for all the mentioned processes. The model offers a tool to study the interactions between biogeochemical processes observed during a bloom of *E. huxleyi*: unbalanced carbon–nitrogen phytoplankton growth leading to depletion of the limiting nutrient, exudation of carbon-rich dissolved organic matter (DOM) under nutrient limitation and formation of TEP induced by accumulation of carbon-rich DOM exudates.

The main innovations of the model consist in 1) the representation of *E. huxleyi* dynamics using an unbalanced growth model in carbon and nitrogen, 2) the gathering of formulations describing typical processes involved in the export of carbon such as primary production, calcification, cellular DOC excretion, TEP formation and viral lyses, 3) the use of an original and validated representation of the calcification process as a function of net primary production with a modulation by the intra-cellular N:C ratio, and 4) a thorough validation of the above-mentioned process thanks to the large diversified data set available in a mesocosm frame. In most of past studies, the validation consists in comparing the simulated (nitrogen) biomass with chlorophyll-a (Chla) values without any validation of calcification and cellular excretion for instance.

The Bergen 2001 mesocosm experiment provided observations on *E. huxleyi* blooms under present, high and low partial pressure of CO_2 (pCO_2). This paper will only focus on simulations of experimental blooms induced in present-day pCO_2 conditions. The objectives are 1) to derive well calibrated formulations of above-mentioned biogeochemical processes 2) to understand the bloom dynamics and 3) to derive a budget of carbon and nitrogen flows during the different phases of the bloom. After a relevant validation of the formulations used in regular conditions, the

aim of future works will be to test these formulations also in acidified and low pCO_2 conditions.

2. Materials and methods

2.1. Experimental settings

The study was carried out between 31 May and 25 June 2001 at the European Union Large Scale Facility (LSF) in Bergen, Norway. Nine outdoor polyethylene enclosures (11 m³, 4.5 m depth) were moored to a raft in the Raunefjorden (60.38°N, 5.28°E). The enclosures were filled with unfiltered, nutrient-poor, post-bloom fjord water, which was pumped from 2 m depth adjacent to the raft. The enclosures were covered by gas-tight tents which allowed for 95% light transmission of the complete spectrum of sunlight, including ultraviolet A and B. The physical settings (temperature, light irradiance, and water turbulence) were similar in the nine enclosures (mesocosms). As the impact of increased atmospheric pCO_2 on calcification and primary production was the main object of the experiment, the pCO_2 inside the mesocosms enclosed atmosphere was controlled continuously during the experiment. The seawater carbonate chemistry was manipulated only at the start of the experiment, before the onset of the bloom, with a bubbling system of CO_2 -enriched air or CO_2 -free air at the bottom of the mesocosms. The triplicate mesocosm treatments represented glacial (~180 ppmV of CO_2), present (~370 ppmV), and future (~700 ppmV) conditions of atmospheric pCO_2 . Mesocosms were numbered from 1 to 9, and mesocosms 4, 5, and 6 correspond to present day pCO_2 conditions. Initial mesocosms seawater was fertilized by adding NO_x^- and PO_4^{3-} . The water column of each mesocosm was actively mixed during the experiment. On 6th June, the fertilization of mesocosms seawater was terminated: NO_x^- concentrations for mesocosms 4, 5 and 6 were respectively 15.4, 14.8, 15.1 $\mu\text{mol L}^{-1}$, and PO_4^{3-} concentrations were respectively 0.46, 0.51, 0.48 $\mu\text{mol L}^{-1}$, with an averaged NO_x^- to PO_4^{3-} (N:P) ratio of 31. Blooms dominated by the coccolithophore *E. huxleyi* occurred simultaneously in all mesocosms and was monitored over a 23 days period. The development of phytoplankton groups other than coccolithophores (*Micromonas* and *Synechococcus*) occurred at the start of the experiment in some mesocosms, the most important was by *Micromonas*. However, available data of PO_4^{3-} and NO_x^- showed that the impact of this bloom on nutrients stocks was not significant. NO_x^- concentrations remained almost unchanged and Chla time-series only showed a slight increase during the *Micromonas* bloom. The rapid collapse of the *E. huxleyi* bloom in the mesocosms was assumed to be due to viral lyses, while grazing was not a significant removal term. The model was designed and calibrated to represent the bloom development under present-day pCO_2 conditions and thus validation is only based on the measurements made in mesocosms numbered 4, 5, and 6 (summarized in Table 1). All variables were measured on a daily basis except for incoming photosynthetic active radiation (PAR), measured hourly.

2.2. Mathematical model

2.2.1. Model structure

The model describes C, N, and P cycling through *E. huxleyi* and the microbial loop. NO_3^- and NH_4^+ are explicitly modelled as well as PO_4^{3-} in order to assess which inorganic nutrient, P or N, was the most limiting for primary production during the experiment. The explicit modelling of P cycling including inorganic and organic forms of P, is required to take into account the capacity of coccolithophores to consume labile and semi-labile dissolved organic phosphorus (respectively DOP_l and DOP_{sl}) as well as PO_4^{3-} (Shaked et al., 2006; Xu et al., 2006; Zondervan, 2007). The DOM is divided into two pools: labile and semi-labile. TA and DIC are explicitly represented in order to obtain a description of DIC cycling and to evaluate the impact of calcification on TA. The model computes pH and pCO_2 from DIC and TA.

Table 1

Physical, chemical and biological variables determined during the Bergen 2001 mesocosm experiment.

Variable	Method	References
λ_{PAR} ($\mu\text{mol Photon m}^{-2} \text{s}^{-1}$)	Spherical quantum sensor	Engel et al. (2005)
T ($^{\circ}\text{C}$)	CTD	Engel et al. (2005)
Salinity	CTD	Engel et al. (2005)
$p\text{CO}_2$ (ppmv)	Equilibrator and Infrared analyser	Delille et al. (2005)
TA ($\mu\text{mol kg}^{-1}$)	Titration	Delille et al. (2005)
DIC ($\mu\text{mol kg}^{-1}$)	Calculated from $p\text{CO}_2$ and TA	Delille et al. (2005)
$p\text{H}_{sws}$ (seawater scale)	Calculated from $p\text{CO}_2$ and TA	Engel et al. (2005)
$\text{NO}_x + \text{NH}_x$ (mmol m^{-3})	Autoanalyser	Engel et al. (2005)
PO_4^{3-} (mmol m^{-3})	Autoanalyser	Engel et al. (2005)
DOC (mmol m^{-3})	Catalytic high combustion	(Engel et al., 2004a,b)
TEP_C (mmol m^{-3})	Colorimetric analysis	(Engel et al., 2004a,b)
PIC (mmol m^{-3})	CHN analyser (TPC–TOC)	Engel et al. (2005)
POC (mmol m^{-3})	CHN analyser	Engel et al. (2005)
PON (mmol m^{-3})	CHN analyser	Engel et al. (2005)
EhV density (part m^{-3})	Microscopy	Rochelle-Newall et al. (2004)
Bacterial density (part m^{-3})	Flow cytometry	Rochelle-Newall et al. (2004)
Chla (mg Chla m^{-3})	Fluorometry	Engel et al. (2005)
<i>E. huxleyi</i> density (cell m^{-3})	Flow cytometry	Engel et al. (2005)

Two forms of PIC are considered: the calcite attached to living cells and the free calcite resulting from dead cells or detached coccoliths. The model includes PCHO and TEP_C dynamics as described by Engel et al. (2004a,b). It also involves a pool of *E. huxleyi* pathogen viruses (EhV)

(Jacquet et al. 2002). This compartment does not sustain a mass flux with the other compartments but its representation is needed to correctly simulate the termination of the bloom.

Since the water column of each mesocosm was actively mixed during the experiment, vertical gradients are neglected and a zero-dimensional model is implemented. A schematic representation of the ecosystem model, indicating the different compartments and flows between them, is shown in Fig. 1. The model state variables (i.e. variables computed by resolving a differential equation), the ordinary variables (i.e. variables directly computed from the state variables or the forcing variables using algebraic equations), the evolution equations for state variables, the equations of biogeochemical processes, and the parameters used in these formulations are listed and defined in Appendix Tables 2, 3, 4, 5 and 6, respectively.

2.2.2. Description of biogeochemical processes

2.2.2.1. Phytoplankton growth and microbial loop. *E. huxleyi* growth is described following an unbalanced growth model in carbon and nitrogen. DIC and nitrogen ($\text{NO}_x^- + \text{NH}_4^+$) uptakes are uncoupled (i.e. the cellular C:N ratio is variable within a certain range, parameters NC_{\min} and NC_{\max} in Appendix Table 6, as described by Tett and Wilson, 2000), while phosphorus ($\text{PO}_4^{3-} + \text{DOP}_L + \text{DOP}_{SL}$) and nitrogen uptakes are coupled following a fixed cellular N:P ratio. The C uptake is limited by DIC availability (Eq. (25)) while the uptake of NO_3^- is inhibited by NH_4^+ availability (Eqs. (27) and (28)). The uptake of PO_4^{3-} is computed from total N uptake following the cellular N:P Redfield ratio (Eq. (29)). The model considers the possibility for *E. huxleyi* to use $\text{DOP}_{L,SL}$ (Eq. (30)). As suggested by Shaked et al. (2006) and Xu et al. (2006), PO_4^{3-} is assimilated preferentially to $\text{DOP}_{L,SL}$ using an inhibition factor for $\text{DOP}_{L,SL}$ uptake. Chla concentrations are modelled as described in Soetaert et al.

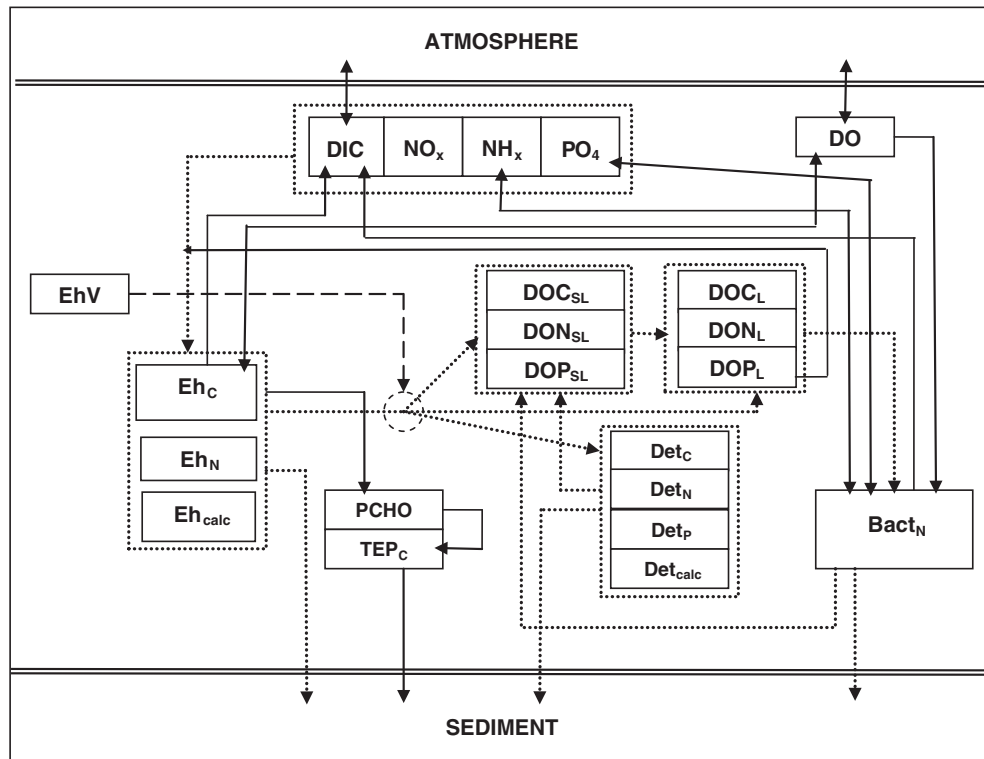


Fig. 1. Schematic representation of the biogeochemical model involving a detailed description of *E. huxleyi* dynamics and the microbial loop. Boxes represent model state variables. Three boxes are related to *E. huxleyi* representing its carbon, nitrogen and calcite contents. The DOM is represented through six boxes: labile and semi-labile DOC, DON and DOP. The particulate detritic matter comprises four boxes (carbon, nitrogen, phosphorus and free calcite). TEP_C and its precursor (acidic PCHO) are represented by specific boxes. Inorganic matter is split into five boxes (DIC , NO_x^- , NH_4^+ , PO_4^{3-} and DO). Arrows represent biogeochemical processes connecting model state variables. If the arrow is dotted, it is a lumped representation of carbon–nitrogen–phosphorus flows. The dash arrow represents the influence of viruses on the *E. huxleyi* mortality.

(2001) and Van Den Meersche et al. (2004), depending on the phytoplankton concentration and the phytoplankton C:N ratio (Eq. (23)). *E. huxleyi* respiration consists in two terms: metabolic respiration and respiration required by cellular activity that is proportional to C uptake (Eq. (26)). As suggested by Anderson and Williams (1998) and Van Den Meersche et al. (2004), bacterial dynamics is formulated using a balanced growth model in C and N. Bacterial growth is sustained by DOM_L and, in certain circumstances (i.e. high C:N ratio of DOM_L), they may also uptake NH_4^+ and PO_4^{3-} . DOM_{SL} needs to be hydrolyzed into DOM_L before being taken up by bacteria.

2.2.2.2. DIC and TA dynamics. As explained by Soetaert et al. (2007), the model uses the total charge $\Sigma[-]$ rather than TA because if one assumes that uptake of ions is compensated by uptake or release of protons then $\Sigma[-]$ is not impacted by changes in the concentrations of NO_3^- , PO_4^{3-} and NH_4^+ . This is not the case for TA (Soetaert et al., 2007). Because we do not consider ΣSO_4 , ΣF , and ΣNO_2 in the model, the relationship between TA and $\Sigma[-]$ is $\text{TA} = \Sigma[-] + \Sigma\text{NH}_4 - \Sigma\text{NO}_3$. Also, DIC and $\Sigma[-]$ are the two model state variables from which pH_{sws} and pCO_2 are computed using dissociation constants of Mehrbach et al. (1973) refitted by Millero (1995). The solubility coefficient of CO_2 at the prevailing temperature and salinity is calculated according to Weiss (1974). For additional details, an extensive description of the carbonate model is provided in Soetaert et al. (2007). At the experimental time scale of one month, the dynamics of CO_2 is mostly determined by biological processes rather than by gas exchange across the air–sea interface. The absence of wind stress on the water surface reduces the diffusion rate of CO_2 across the air–sea interface to molecular diffusion (Wanninkhof, 1992).

2.2.2.3. Carbon exudation and TEP_C formation. *E. huxleyi* exudates DON_L and DOC_L through passive leakage (Eqs. (35), (36) and (37)), as in Van Den Meersche et al. (2004). *E. huxleyi* also exudates DOC_L and DOC_{SL} through active excretion. This last process is an active mechanism consisting in the exocytosis of high molecular weight substances mainly composed of organic carbon (PCHO) (Eq. (38)). This release of DOC reflects the carbon over-consumption. As described by Engel et al. (2004a,b), TEP_C formation is strongly linked to the cellular DOC excretion: a part of which (parameter $L_{t_{\text{ex}}}$ in Table 6) consists in acidic PCHO able to coagulate, making the precursor of TEP_C . These acidic PCHO may also be directly adsorbed by existing TEP_C (Eq. (5)). Coagulation and adsorption of acidic polysaccharides are modelled following equations given by Engel et al. (2004a,b). Also, the model state variable PCHO refers to acidic PCHO which is the fraction of cellular DOC excretion able to coagulate and acting as TEP_C precursor.

2.2.2.4. Calcification. The model assumes that the calcifying activity of *E. huxleyi* is a structural cellular requirement induced by the normal growth of the cell. Following mesocosms experimental observations, the most efficient calcification is obtained when the cellular carbon growth is sustained under limited nutrients condition. Accordingly, the model describes the calcification as the combination of two terms (Eq. (39)): the main term is proportional to the net primary production (computed as the difference between DIC assimilation and respiration by *E. huxleyi* cells) using a constant calcite to cellular C ratio. This term is multiplied by a function of the cellular N:C ratio disabling calcification when that ratio is equal to its maximum value. In addition, the model considers a minor term representing the permanent basal calcification as a function of the phytoplankton carbon biomass. Calcification leads to the production of coccoliths constituting the attached calcite. A part of these coccoliths are lost by detachment, providing the free calcite pool (Eq. (40)). Due to a protective carbohydrates envelop around the *E. huxleyi* cell (Godoi et al., 2009), attached calcite is preserved from dissolution in the coccosphere. Only free calcite is allowed to dissolve when the saturation state with respect to calcite (Ω_{cal}) drops below unit.

2.2.2.5. Viral lysis. Isolated, viruses have no capability of multiplication. They are only produced within infected phytoplankton cells and spread out when infected cells die. Hence, the model considers that the growth of the viral population is driven by the fraction of *E. huxleyi* mortality caused by viral infection (variable $R\eta_{\text{vir}}$ in Eq. (44)). A constant spread-out coefficient is applied to compute the number of new viruses released by dying infected cells (Jacquet et al., 2002). Once produced, the viruses keep their infecting potential for a limited time. The structural proteins of viruses are continuously degenerating, making an infection impossible after a certain time. This process is similar to a mortality affecting the viral population at a constant rate. The viral induced mortality is an additional term to the senescent mortality of *E. huxleyi*. The mortality caused by viruses is determined by a threshold function based on the encounter probability between viral agents and cellular hosts (Eqs. (43) and (44)) that rely on cell and virus densities.

2.2.2.6. Sedimentation. Despite the permanent mixing applied to the water column during the experiment, deposits were observed at the bottom of the mesocosms, as corroborated by the computation of carbon losses in the water column (Delille et al., 2005). Due to the small depth of the mesocosm (4.5 m) and the continuous bubbling applied during the whole experiment, we do not model explicitly the aggregation process between particulate materials. We impose rather constant sinking speeds for *E. huxleyi* cells, free PIC, TEP_C , and detritus (Table 6). These sinking speeds were obtained from literature for *E. huxleyi* cells and free PIC (Paasche, 2002), or calibrated from the experimental measurements for TEP_C and detritus. As explained in Section 2.2.4, this calibration exercise gives a small value for the sinking speed for TEP_C more than one order of magnitude lower than that for detritus. To justify the use of a low sinking speed for TEP_C , we refer notably to the work of Engel et al. (2004a,b) who were able to reproduce the TEP_C dynamics observed during a mesocosm experiment considering the aggregation of PCHO and ignoring the vertical sinking of TEP_C . This can be justified by the fact that TEP_C does not sink gravitationally (Engel and Schartau, 1999) but becomes attached to sinking particles and settles within aggregates. The model does not consider the degradation of the settled organic material, i.e. there are no fluxes of DIC and nutrients from the bottom deposit to the mesocosm water column.

2.2.3. Model implementation and forcings

Initial conditions for most of model state variables were directly obtained from the experimental data: DOC, POC, PON, TEP_C , TA, DIC, PIC, NO_x^- , PO_4^{3-} , viral, bacterial, and *E. huxleyi* abundances. Initial organic carbon detritus (Det_C) was computed as the difference between the measured POC and the sum of TEP_C and *E. huxleyi* carbon biomass. Conversion factors were used to derive *E. huxleyi* C biomass and bacterial N biomass from their respective abundances. The organic C content for bacteria was fixed to $1.0 \cdot 10^{-12}$ mmol C bact^{-1} as proposed by Goldman et al. (1987) and the bacterial C:N ratio is fixed to 4. The cellular organic C content of *E. huxleyi* is calculated during the limited nutrients phase (day 10 to day 15) as the averaged ratio of the time variation of POC to the time variation of the abundance of *E. huxleyi* i.e. $(d[\text{POC}]/dt)/(d[E. huxleyi]/dt)$. During this period, the increase of the POC concentration is largely dominated by the *E. huxleyi* development. Results given for this ratio are quasi similar for the three mesocosms. The mean value of $2.0 \cdot 10^{-9}$ mmol cell^{-1} was used during the entire simulation in order to convert the modelled C biomass into cellular abundance.

2.2.3.1. Forcing variables. Measurements of PAR at the surface were available hourly. An averaged value of PAR at half depth is calculated from the daily observation of the PAR profile and is used for the computation of the DIC uptake associated to photosynthesis. Other forcing variables measured daily during the experiment were temperature, salinity and pCO_2 in the enclosed atmosphere. Since we are only interested in

representing the dynamics of *E. huxleyi*, in order to minimize the effect of the *Micromonas* bloom on the DIC, TA, and nutrients, a nudging is applied for these variables, from day 1 to day 5.

The model was implemented in FEMME (Flexible Environment for Mathematically Modelling the Environment, <http://www.nioo.knaw.nl/node/513>, Soetaert et al. (2002)). The model was integrated over the whole duration of the experiment (i.e. 23 days). Numerical computations were carried out using explicit Euler integration with a time step of 14 min. Model outputs were stored hourly.

2.2.4. Specific parameters and model calibration

Model parameters are fine-tuned using an identifiability analysis. This allows selecting a parameter set that is identifiable with the available data. The model is found to be the most sensitive to $R_{\mu C}$, K_{λ} , Eh_{SS} , and th_{EhV} . These most sensitive parameters in addition with other parameters ($R_{\mu NOx}$, F_{Ccalc} , P_{sil} , $R_{\eta bac}$, η_{virmax} , and R_{η}) are then calibrated with an automatic calibration procedure based on Levenberg–Marquardt algorithm. The variation range for parameters values is fixed between $\pm 20\%$ and $\pm 50\%$ of their nominal values following the uncertainty affecting the parameter. The procedure is repeated till convergence (Brun et al., 2002). *E. huxleyi* DIC uptake rate at 20 °C ($R_{\mu C}$) is fixed to 0.11 h^{-1} in agreement with reported values ranging between 0.09 and 0.12 h^{-1} (Paasche, 2002; Merico et al., 2004). The parameter R_{calc} controlling the basal calcification rate is obtained by fitting during the non-limited nutrients phase of the bloom, giving a value of 0.001 h^{-1} . The parameter F_{Ccalc} controlling the ratio between *E. huxleyi* calcite production and its organic C growth is derived from the experimental data, giving a value of 1.9. The calibration procedure proposed a sinking speed of 0.015 m h^{-1} for the *E. huxleyi* cells. The sinking speed for $Det_{C,N,P}$ and TEP_C was linearly fitted in order to reproduce experimental observations concerning the C losses in the mesocosms. The rates are 0.04 m h^{-1} and 0.002 m h^{-1} for $Det_{C,N,P}$ and TEP_C respectively.

3. Results and discussion

The following results concern the application of the model in present-day pCO_2 conditions ($410 \mu\text{atm}$). The Bergen 2001 mesocosm experiment provided a diversified data set essential to test jointly several formulations about cellular processes of *E. huxleyi*. Observed TA and DIC allow the validation of parameters concerning calcification. Observed DIC and TEP_C allow the validation of parameters concerning DOC excretion and TEP_C formation. Observed NO_3^- and PO_4^{3-} allow testing the formulation of inorganic nutrient uptakes by *E. huxleyi*. Observed DIC, nutrients and Chla allow assessing the dynamics of the uncoupling of C and N.

3.1. General description of model results: analysis of the three phases composing the bloom

Model results show that the general pattern of carbon and nitrogen fluxes varies according to three phases. A first phase (between days 5 and 12) is characterised by the development of *E. huxleyi* population without any nutrients limitation. DIC and other inorganic nutrients are largely consumed and the *E. huxleyi* abundance increases. During the second phase (between days 12 and 16), PO_4^{3-} stock becomes depleted and the bloom of *E. huxleyi* is sustained under inorganic nutrients limitation. Uncoupling between DIC and nutrients consumptions is observed as DIC is still consumed albeit nutrients uptake has stopped. During this second phase, *E. huxleyi* abundance keeps on increasing, reaches its maximum and then maintains a quasi-constant value. Finally, the third phase (between days 16 and 23) consists in a fast decrease of *E. huxleyi* abundance consequent to a viral attack rather than a natural cellular senescence.

The development of the *E. huxleyi* population during the first phase is observable through the exponential increase of both cellular abundance

and Chla variables. All particulate variables (POC, PON and POP) also increase and DIC slowly decreases. This decrease of DIC is quite moderate because the *E. huxleyi* abundance is not high enough to sustain a strong DIC uptake. Both NO_3^- and PO_4^{3-} are consumed following the constant N:P ratio imposed in the model. TA remains quasi unchanged close to its initial value, reflecting the absence of any significant calcifying activity during this nutrients non-limited phase. This is also attested by the unchanged PIC which remains at a quasi-zero level till the end of the first phase. TEP_C slightly increases in the early phase consequent to a coagulation of the initial stock of PCHO. After this coagulation event, TEP_C keeps a quasi-constant value till the end of the first phase. C:N ratio remains quasi unchanged close to its initial value of 6 attesting the Redfield balanced uptakes of DIC and nitrogen (NO_3^- and NH_4^+) during this first phase. Stock of NH_4^+ becomes quasi totally consumed at the end of the first phase.

The second phase is triggered by the exhaustion of PO_4^{3-} with labile and semi-labile DOP stocks, which are consumable by *E. huxleyi*. This occurs while NO_3^- is still available and thus P is the element limiting the development of the *E. huxleyi* population in these mesocosm experiments. Due to the coupling of N and P uptakes, the unavailability of P causes the cessation of NO_3^- and NH_4^+ uptakes. DIC is still consumed due to the uncoupling of C and N uptakes. This second phase is thus characterised by the sharp increase of the C:N ratio. The development of *E. huxleyi* population becomes only sustained by carbon provision. Both PON and POP are decreasing while POC keeps increasing. This is also reflected by the collapse of Chla, computed from the cellular nitrogen biomass, while the *E. huxleyi* abundance, computed from the cellular carbon biomass, keeps increasing. High cellular C:N ratio constrain the DIC uptake making that the increase of *E. huxleyi* abundance stops one day after the nutrient exhaustion. The DIC uptake is then able to compensate the carbon losses due to respiration, but is not anymore able to sustain a growth of the *E. huxleyi* population. Indeed, the *E. huxleyi* abundance becomes quasi constant and keeps its maximum value till the end of this second phase. Another consequence of this elevated cellular C:N ratio is the triggering of calcification and cellular DOC excretion. The decrease of TA is concomitant with the moment of inorganic nutrients (PO_4^{3-}) depletion, in parallel with an increase of PIC, reflecting the mobilisation of bicarbonate ions to produce calcite. A sharp inflexion is also observable for TEP_C in the early second phase. This TEP_C increase is consequent to the coagulation of the huge quantity of DOC excreted by *E. huxleyi* growing under nutrient limitation. DOC and DON significantly increase during this second phase. DOC and DON stocks are mainly provided by the dissolution of POC and PON accumulated during the previous development of the *E. huxleyi* population.

The sharp increase of the viral density around day 16 initiates the third phase. Viruses are present since the beginning of the simulation but their multiplication requires high *E. huxleyi* abundance. These viruses become observable and cause significant *E. huxleyi* mortality only a few days after the abundance has reached its maximum. The enhanced cellular mortality due to viral lysis is responsible for the collapse of the *E. huxleyi* abundance observable in this third phase. Cellular activities such as calcification and DOC excretion are not directly impacted by the viruses. However, their external manifestations through the PIC and TEP_C productions become limited by the diminution of the *E. huxleyi* abundance. This is reflected by the stabilization of TA and DIC. In addition, TEP_C stops increasing and remain quasi constant due to the low sedimentation rate imposed in the model. PIC and POC variables reach their maximum in the early third phase and then decrease sharply due to the sinking of these particulate materials. Viral density peaks three days after the beginning of the third phase, and then collapses rapidly. This is due to the low *E. huxleyi* abundance at the end of the third phase leading to a dramatic decrease of the production rate of new viruses.

3.2. Comparison of model outputs and experimental observations

In this section, we will compare model outputs with observations collected during the mesocosm experiment. In Section 3.3, we will discuss and explain the differences between both.

3.2.1. Phytoplankton growth

Modelled and observed *E. huxleyi* abundances are globally time-phased: both maxima are reached around day 16 (Fig. 2). However, abundance tends to be slightly overestimated in the model. The model gives a good representation of POC corresponding to the sum of

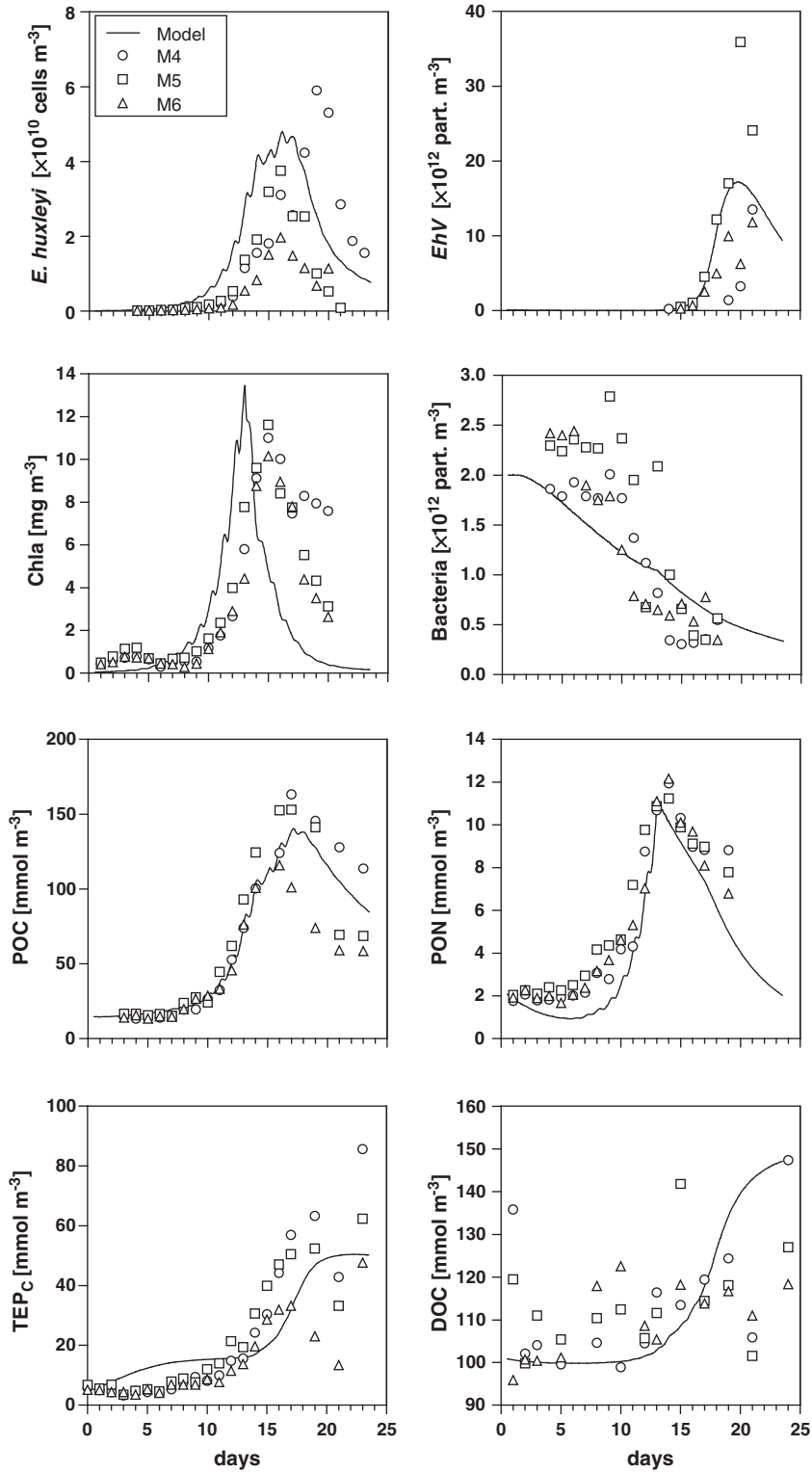


Fig. 2. Evolution of *E. huxleyi* abundance, viral density (EhV), Chla, heterotrophic bacteria, POC, PON, TEP_c, and total DOC. (continuous line: model, circles: mesocosm 4, triangles: mesocosm 5, and crosses: mesocosm 6). The first phase of the bloom is evidenced by the increase of the *E. huxleyi* abundance, Chla, POC and PON. The second phase is characterised by the onset of TEP formation and the decrease of PON consequent to the growth under limited-nutrient conditions. The third phase of the bloom is notable by the sharp collapse of the *E. huxleyi* abundance and the raise of the viral density.

E. huxleyi carbon biomass, carbon detritus and TEP_C . Modelled and observed POC are very close till the moment of nutrients limitation. After, observed POC values between mesocosms become quite divergent. The model follows the decreasing trend of the observations and remains within the range (Fig. 2). Modelled and observed PON are well time-phased: both peak on day 14 (Fig. 2). The model tends however to underestimate the amount of PON during the first phase of the simulation. Modelled Chla is in the range of observations although it peaks slightly earlier in the model and then decreases faster than in the observations (Fig. 2). The slight increase of Chla visible in the observations during the first 5 days of the experiment is due to the development of other phytoplankton groups (*Micromonas* and *Synechococcus*). The Chla peak associated to these phytoplankton groups represents only a tenth of the Chla peak observed during the bloom of *E. huxleyi*. These groups are not modelled. Modelled NO_x^- and PO_4^{3-} are in agreement with the observations (Fig. 3). The observations show that phosphorus is the limiting nutrient for phytoplankton growth in all mesocosms. The model represents the phosphorus limitation: PO_4^{3-} as well as labile and semi-labile DOP are entirely consumed by *E. huxleyi* around day 10.

3.2.2. Microbial loop

Model and observations show a global decrease of the bacterial population with a quasi-constant rate, evolving from initially $3.0 \cdot 10^{12}$ to $0.5 \cdot 10^{12}$ cells m^{-3} at the end of the experiment (Fig. 2). Bacterial growth highly depends on the availability of DOM_L mainly provided by the phytoplankton mortality. Until day 16, labile organic substrates availability is not sufficient for an effective bacterial growth due to the low mortality rate of *E. huxleyi* cells. The sharp rise of phytoplankton mortality due to viral lyses after day 16 leads to a massive input of DOM_L . However, bacterial growth is then constrained by the high C:N ratio of the DOM released during this phase of the experiment. Consequently, bacteria shift to a competitive behavior with phytoplankton for inorganic nitrogen and phosphorus. Observed DOC shows a global increasing pattern, from initially 100 to 120 $mmol m^{-3}$ at the end of the experiment. However, this pattern is not clearly depicted in the observations due to large differences between the three mesocosms (Fig. 2). The modelled DOC remains however within the range of the observations although the increase of DOC is much sharper in the model than in the observations. This increase is consequent to the enhancement of *E. huxleyi* mortality due to viral lyses after day 16.

3.2.3. Viruses

The model succeeds to reproduce the multiplication of viruses: modelled and observed viral densities are close and time-phased (Fig. 2). In the model, the multiplication of viruses is triggered around day 16, as a consequence of the elevated *E. huxleyi* abundance prevailing at the end of the limited nutrients phase of the bloom. Before day 16, the modelled viral density remains at a quasi-zero level. This is in agreement with the observations from all the three mesocosms where the viral density sharply increases only between day 15 and day 17. The viral density peaks around day 19 in the observations and the model, reaching a value of $15 \cdot 10^{12}$ part m^{-3} . This corresponds to the maximal viral density observed in mesocosms 4 and 6. After day 20, the observations show a sharp decrease of the viral density, falling to zero at the end of the experiment. The effective presence of viruses is thus restricted to a narrow period of three days, between day 17 and day 20. Compared to the observations, the modelled viral density decreases with a smoother slope after the peak, and viruses are still present at the end of the simulation.

3.2.4. DIC and TA

The observed DIC decreases from the beginning of the experiment. This trend is clearly enhanced after day 10 due to the massive development of the *E. huxleyi*. Phytoplankton groups other than

E. huxleyi (i.e. *Micromonas*) do not induce a marked impact on observed DIC during the early experiment. Till the moment of nutrients limitation, the decrease of DIC is not accompanied by a decrease of TA, revealing that DIC uptake is only due to primary production and not to calcifying activity. The observed DIC in the 3 mesocosms begins to diverge after day 15: in mesocosms 5 and 6, DIC stops decreasing, while DIC keeps on decreasing in mesocosm 4. Modelled DIC follows the observations trends and remains within their range during the whole simulation (Fig. 3). The DIC concentration at the end of the simulation is in agreement with the observations. However, observed DIC increases slightly in the three mesocosms during the last days of the experiment, and this pattern is not reproduced by the model.

The variation of TA reflects the uptake of bicarbonate ions sustained by *E. huxleyi* for the production of calcite. Observed TA remains quasi unchanged in the three mesocosms from the beginning of the experiment till the moment of PO_4^{3-} depletion around day 12 (Fig. 3). A sharp inflexion of the observed TA time-series is then visible on day 13 showing that the *E. huxleyi* calcification is suddenly triggered. Observed TA keeps on decreasing sharply for the next 4 days. Modelled TA remains within the range of the observations although these become highly variable between the 3 mesocosms during the viral termination of the blooms. The TA scenario that is presented by our simulation is in agreement with the viral lysis observed in mesocosm 5 (squares) in Figs. 2 and 3. The decrease of the modelled TA strongly slows down after day 18 but is maintained till the end of the simulation. The final modelled TA is close to the averaged final observed TA.

3.2.5. DOC excretion and TEP_C formation

Observed TEP_C increases slightly but continuously since the beginning of the experiment. This suggests the existence of TEP precursor in the environment, possibly produced by the smaller bloom of *Micromonas* that occurs at the early beginning of the experiment. Observed TEP_C shows a clear inflexion around day 13, when PO_4^{3-} becomes depleted and induces nutrient limitation for primary production. Due to the balanced phytoplankton growth between nitrogen and phosphorus, the cessation of PO_4^{3-} uptake also stops nitrogen assimilation and increases the cellular C:N ratio. Elevated C:N ratio enhances cellular excretion of TEP precursor (PCHO), whose coagulation increases the amount of TEP_C . The model reproduces that overall evolution but tends to overestimate TEP_C early in the simulation (Fig. 2). Most of the modelled TEP_C is produced during the nutrient limited phase of the bloom, and the slopes of observed and modelled TEP_C time-series are then quite similar.

3.3. Discussion and analysis of processes

3.3.1. *E. huxleyi* dynamics: unbalanced growth

An unbalanced growth model for carbon and nitrogen appears to be adapted to represent the development of *E. huxleyi* observed in the mesocosm experiment. Observed time-series reveal that pCO_2 keeps on decreasing at the same rate during two days after the occurrence of PO_4^{3-} depletion. This highlights the decoupling between the uptakes of NO_x^- and DIC dedicated to photosynthesis by *E. huxleyi*, as far as PO_4^{3-} and NO_x^- uptakes are balanced. The depletion of PO_4^{3-} prevents any assimilation of NO_x^- that remains at a concentration of 0.5 $mmol m^{-3}$ until the end of the experiment. This leads to an increase of the cellular C:N ratio which will have an impact on several cellular processes: the DIC fixation into living biomass becomes constrained and the cellular DOC excretion is enhanced. This unbalanced mechanism allows reproducing the general pattern of the *E. huxleyi* development observed during the mesocosm experiment.

A fixed cellular organic carbon content coefficient is used to convert the modelled *E. huxleyi* carbon biomass into abundance. The cellular organic carbon content is linked to the size of the cell. This size

may be decreasing when the cellular growth is sustained under limited nutrient conditions (Engel et al. 2008) leading to a decrease of the cellular organic carbon content. However, since no precise information regarding the potential size of the cells is available from the mesocosm experiment, the comparison between model results and observations of *E. huxleyi* abundances relies on the assumption

that the cellular organic carbon content of *E. huxleyi* cells remains unchanged during the whole experiment and fixed as explained in Section 2.2.3.

The modelled Chl *a* starts to increase and peaks earlier compared to the observations. Afterwards, modelled Chl *a* decreases faster than the observations. This difference can be explained by the fact that, in the

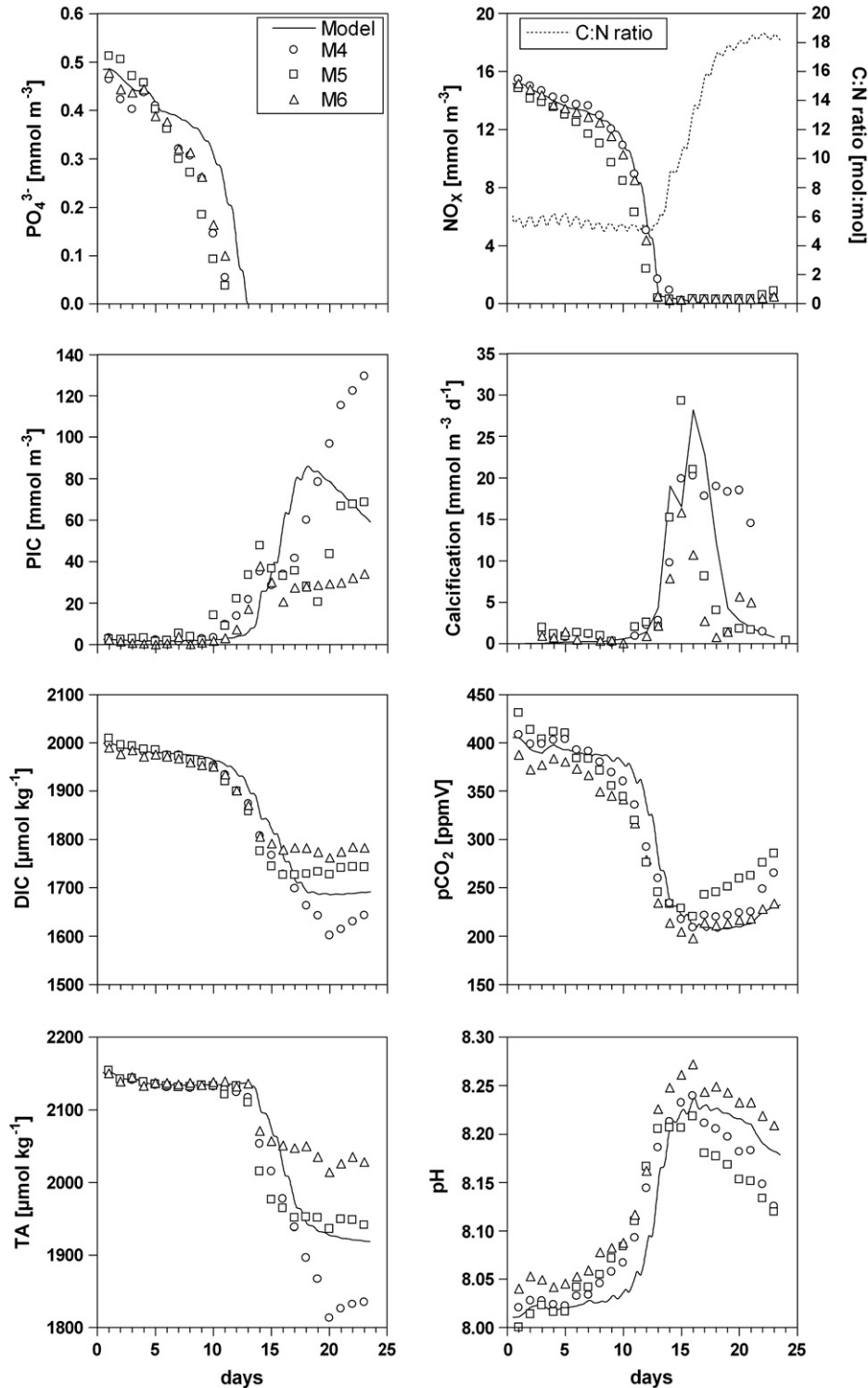


Fig. 3. Evolution of PO_4^{3-} , NO_x^- (dashed line corresponds to simulated cellular C:N ratio), PIC, daily calcification rate, DIC, pCO_2 , TA and pH (continuous line: model, circles: mesocosm 4, triangles: mesocosm 5, and crosses: mesocosm 6). The first nutrient to be depleted is PO_4^{3-} shifting the *E. huxleyi* growth to limited-nutrient conditions. The DIC uptake goes on after the PO_4^{3-} limitation. Due to the cellular N:P coupling, the PO_4^{3-} limitation leads to a raise of the cellular C:N ratio. The onset of the calcifying activity, visible through the decrease of TA, is concomitant with the raise of the cellular C:N ratio.

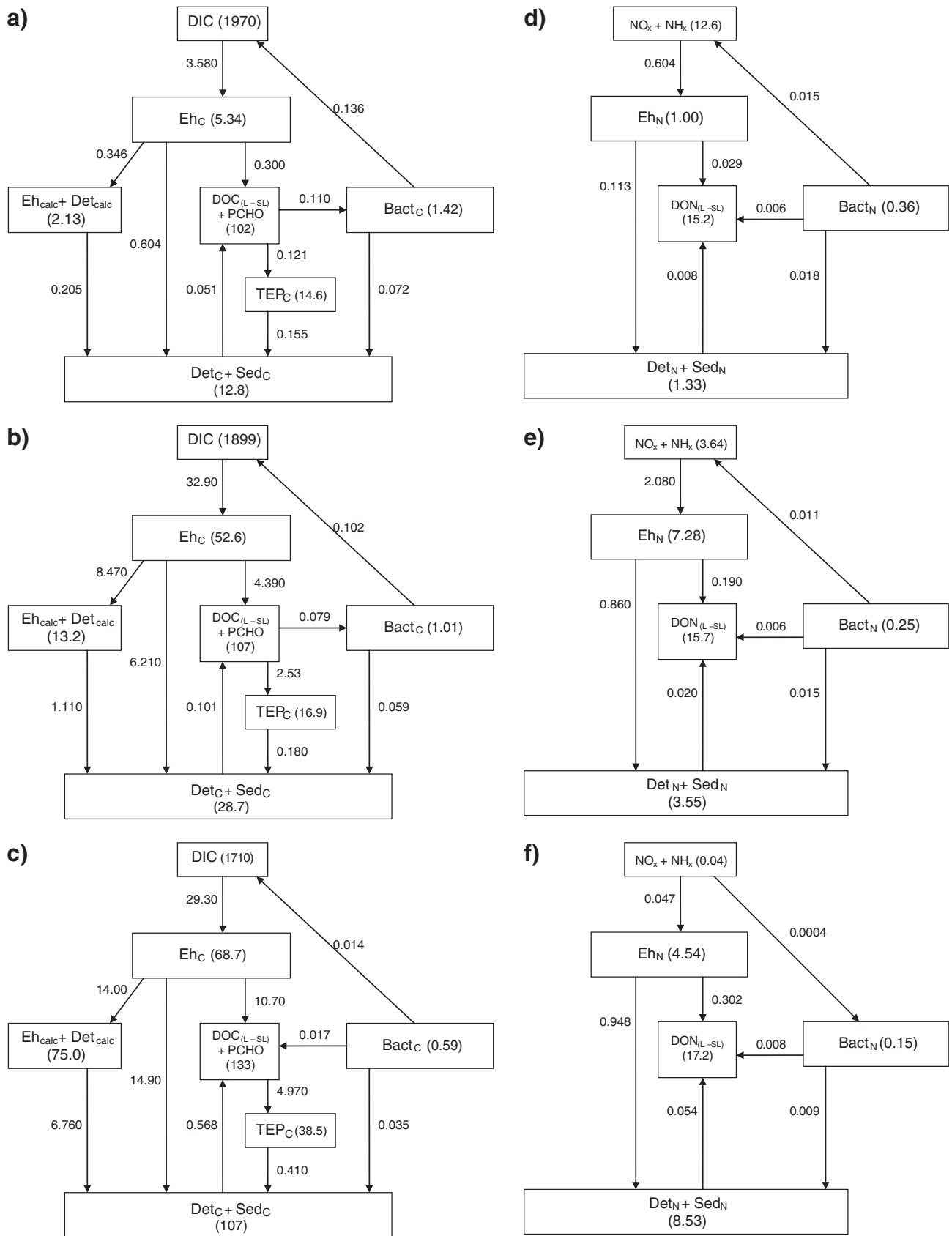


Fig. 4. Carbon and nitrogen budgets derived from the model over three phases between day 5 and day 20. Values on the arrows are fluxes in $mmol\ m^{-3}\ day^{-1}$. Values inside boxes are daily averaged stocks for the modelled variables in $mmol\ m^{-3}$. During the first phase (days 5–12), the bloom development occurs without nutrient limitation. The second phase starts on day 12 after the depletion of PO_4^{3-} and the bloom shifts to nutrient-limited conditions. The third phase starts on day 16 and is characterised by the viral termination of the bloom.

final phase of the bloom, the major part of Chla observed in the water column is not included in living cells while model computes Chla only from living cells. Besides, in the model, Chla is not dynamically computed but is deduced from phytoplankton carbon biomass (Eq. (23)). These two reasons may explain the underestimation of modelled Chla after the collapse of the *E. huxleyi* population around day 16.

The model does not consider diagenetic processes in the deposits on the bottom of the mesocosms. Processes that affect DIC, such as the bacterial respiration or CaCO_3 dissolution, are only represented in the mesocosm water column. Also, material that reaches the bottom is not degraded and is definitely lost. This could explain the divergence between modelled and observed evolutions of DIC and pCO_2 from day 18 till the end of the experiment: observed DIC and pCO_2 values increase slightly, probably due to degradation of organic carbon in bottom deposits, while the model does not reproduce these trends.

3.3.2. Calcification

Following the formulation used in the model, calcification is conjointly determined by the evolution of the cellular C:N ratio and by the intensity of the primary production. The dynamics of calcification shown by the model is in agreement with the observations. The decrease of modelled TA occurs within a narrow time window (between days 12 and 16) concomitantly with the nutrient exhaustion and the parallel raise of the cellular C:N ratio (Fig. 3). In the observations, the production of calcite, reflected by the decrease of TA, starts around day 12 and ends on day 16. Most of the calcite is produced during only 4 days, which implies high daily calcification rates during this period. Modelled rates are in agreement with the estimates of Delille et al. (2005) based on the change of TA corrected for inorganic nutrient assimilation (Fig. 3). The model shows a good representation of the calcification onset: modelled and observed PIC rise concomitantly, as it is also attested by the decrease of TA. This good agreement suggests that the triggering of the calcifying activity is mainly dependent on the cellular C:N ratio. Decoupling between DIC and nitrogen uptakes is thus necessary to represent a good time-phasing of the onset of calcification. Whether the cellular C:N ratio controls the initiation of the calcification, the function of primary production introduced in the formulation is able to determine the evolution and the termination of the calcification. Using such a formulation, calcification is maintained as long as primary production of *E. huxleyi* occurs. The delay between the onset of calcification and the peak of *E. huxleyi* abundance suggests that a representation of calcification should not be based only on the cellular C biomass. On the contrary, the good agreement between model and the observations shows that an accurate representation of the calcification dynamics is obtained with a formulation linked to primary production and nutrient limitation.

Fig. 5 compares modelled TA and calcification rates using three different formulations for the representation of calcification. A first formulation is based only on the *E. huxleyi* carbon biomass with a calcification rate optimized to 0.01 h^{-1} (identified in Fig. 5 as Model a). This formulation anticipates the onset of the calcifying activity. The calcification is also sustained for too long leading to a clear underestimate of the TA at the end of the simulation. The second formulation applies the formulation used in the model but without the modulation by the cellular N:C ratio, thus using only the term F_{calc} (net primary production) (identified in Fig. 5 as Model b). This formulation satisfactorily represents the intensity of the calcification. The modelled TA is indeed in the range of the observations at the end of the simulation. However, the weakness of this formulation is that it anticipates again the onset of the calcifying activity: modelled TA decreases three days before the observed TA. This leads to an underestimation of the TA during the nutrient non-limited phase of the bloom. The third formulation (function of net primary production and modulated by cellular N:C ratio as used in the present study, same

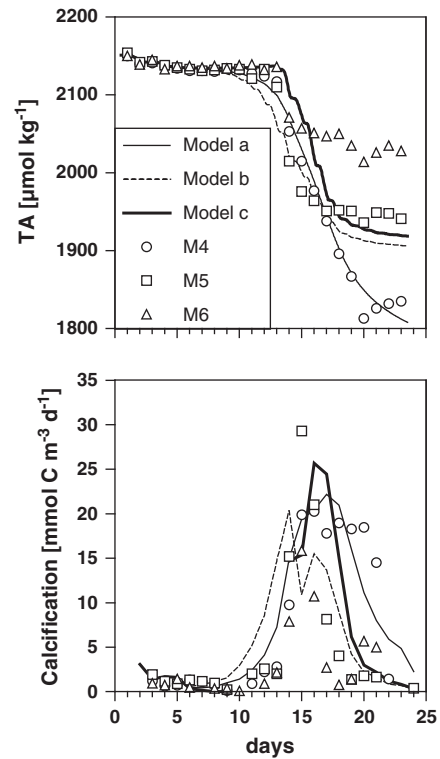


Fig. 5. Comparison of TA and calcification rates simulated using three different formulations of calcification: a) as function of *E. huxleyi* carbon biomass (with param R_{calc} adapted to 0.01 h^{-1}); b) applying the formulation used in the model but ignoring the modulation of the cellular N:C ratio, thus using only the term F_{calc} (net primary production); and c) as used in the model (function of primary production modulated by cellular N:C ratio, same as in Fig. 3).

as in Fig. 3, identified in Fig. 5 as Model c) provides the best timing for the onset of calcification, and calcification rate peaks on day 16 in fair agreement with the measured rates.

3.3.3. DOC excretion and TEP_C dynamics

Products of the cellular DOC excretion are shared between the TEP_C precursors (i.e. acidic PCHO) and the labile DOC pool. In the early phase of the experiment, observations show that TEP_C is slightly produced but the major formation of TEP_C is only triggered on day 12, concomitantly with the onset of calcification. However, in the model, TEP_C increases already significantly during the beginning of the simulation. This difference of behavior between model simulation and observations can be explained as follows. As explained in section “model description”, the modelled PCHO is considered to be exclusively acidic PCHO resulting from cellular DOC excretion and having coagulating properties. In order to initialize this state variable, we use observations of PCHO for which it is not possible to identify the acidic coagulating part. Most of this initial stock of PCHO results from the remaining polysaccharides produced by a previous bloom (in the fjord source water). Also, we overestimate the initial stock of acidic PCHO leading to an early overproduction of TEP_C compared to observations. Then, as PO_4^{3-} becomes depleted and the *E. huxleyi* cellular C:N ratio begins to increase, the model sharply enhances cellular DOC excretion and thus the provision of acidic PCHO in the water column, leading to the major formation of TEP_C . In the final part of the experiment, the observations show a sudden decrease of TEP_C after day 18, probably due to a massive aggregating event between TEP_C and detritus, and their removal from the water column. The model does not however represent any aggregating process and fails to represent this feature.

3.3.4. Virus

Observations show that the collapse of *E. huxleyi* abundance and the raise of viral density are concomitant, attesting the viral termination of the bloom. This confirms that the impact of enhanced cellular mortality due to interaction between cells and viruses has to be considered in confined environments. The onset of the viral multiplication is driven by the promiscuity between viruses and cellular hosts. That promiscuity is highly dependent of the *E. huxleyi* abundance. This underlines the importance of the cellular carbon content making the conversion of the *E. huxleyi* carbon biomass into abundance. An overestimation of the cellular carbon content leads to an underestimation of the cellular abundance which can delay the viral multiplication. Observations show that the multiplication of viruses suddenly stops after day 20. A possible reason is that the rate of virus production became lower than the rate of viral degeneration. The abundance of *E. huxleyi* dropped below the threshold required to maintain a sufficient promiscuity between viruses and hosts, a necessary condition for a high infecting rate. Another process enhancing the termination of the viral attack may also be the removal of viruses scavenged by aggregates, as export is enhanced at the very end of the experiment (a sudden decrease of both TEP_C and POC concentrations is observed after day 18). In the model, the viral abundance peaks around the same day as in the observations (day 20). Afterwards, the modelled viral abundance decreases at lower rate compared to the observations. This is unrelated to the parameters describing the viral dynamics as far as they succeed to represent the triggering and increasing phase of the viral event. Actually, the model does not involve any representation of aggregation. This contributes to overestimate many variables at the end of the experiment, organic particles and TEP_C, as well as the abundance of viral particles.

3.4. Carbon and nitrogen fluxes inside the mesocosms

The model was used to derive carbon and nitrogen budgets for the three phases composing the bloom and described in Section 3.1. The first phase (nutrient non-limited phase) extends from day 5 till the complete consumption of PO₄³⁻ on day 12. The second phase (nutrient-limited phase) extends from day 12 till the collapse of the *E. huxleyi* population due to the viral attack around day 16. The third phase (viral termination phase) extends from day 16 till the end of the experiment. Fig. 4 shows for each phase the daily averaged carbon and nitrogen fluxes between the model compartments.

3.4.1. First phase: nutrient non-limited phase (days 5–12)

The nutrient non-limited phase is characterised by carbon and nitrogen fluxes, from DIC and (NO_x⁻ + NH₄⁺) compartments to the *E. huxleyi* carbon and nitrogen biomass compartments, sustained with a relative ratio of 6 in agreement with the Redfield value. The major part (66%) of the total *E. huxleyi* DIC uptake (3.58 mmol C m⁻³ day⁻¹) is used to increase the *E. huxleyi* carbon biomass. Minor parts of the DIC uptake, about 9% (0.346 mmol C m⁻³ day⁻¹) and 8% (0.30 mmol C m⁻³ d⁻¹), are related, respectively, to free and attached calcite production and to any form of cellular DOC excretion (passive leakage and active excretion). Consequently, calcite and TEP_C production are very low during this first phase of the bloom. The remaining part of the DIC uptake (17% or 0.60 mmol C m⁻³ day⁻¹) consists in detritus accumulation in the water column or sedimentation. In parallel to the carbon fluxes, the nitrogen flux resulting of (NO_x⁻ + NH₄⁺) uptake is able to maintain a cellular C:N ratio close to 5. During this phase, the net mesocosm production is positive with *E. huxleyi* gross primary production exceeding the community respiration. The total flux of carbon that goes from the *E. huxleyi* compartment to detritic matter and sediment is 0.97 mmol C m⁻³ day⁻¹: 0.21 mmol C m⁻³ day⁻¹ (21%) in inorganic form (free and attached calcite) and 0.60 +

0.16 mmol C m⁻³ day⁻¹ (79%) in organic form (sinking cells, cellular mortality and TEP).

3.4.2. Second phase: nutrient-limited phase (days 12–16)

After day 12, PO₄³⁻ is entirely consumed. The flux from NO_x⁻ is unable to maintain a cellular C:N ratio of 6 and *E. huxleyi* shifts into an unbalanced growth phase regarding carbon and nitrogen uptakes. The flux from DIC to the *E. huxleyi* compartment contributes to increase the *E. huxleyi* carbon biomass. However, only 42% of the total DIC uptake (32.90 mmol C m⁻³ day⁻¹) is now dedicated to the carbon organic biomass growth. This second phase of the bloom is characterised by the onset of calcification as 26% (8.47 mmol C m⁻³ day⁻¹) of the DIC uptake is used to produce calcite. TEP_C production is also enhanced as a consequence of the increase of cellular DOC excretion, consisting in 13% (4.39 mmol C m⁻³ day⁻¹) of the DIC uptake. The cellular DOC excretion increases the DOC pool in the mesocosm causing the raise of the DOM C:N ratio. This reduces the excretion of NH₄⁺ and remineralization of PO₄³⁻ by bacteria, making the limited nutrients condition more severe in the community. More than 7.50 mmol C m⁻³ day⁻¹ constitutes the total flux of carbon that goes from the *E. huxleyi* compartment to detritic matter and sediment: 1.11 mmol C m⁻³ day⁻¹ (15%) is in the form of PIC and 6.21 + 0.18 mmol C m⁻³ day⁻¹ (85%) is in organic carbon.

3.4.3. Third phase: viral termination phase (days 16–23)

The multiplication of viruses and the sharp decrease of the *E. huxleyi* density characterize the termination of the bloom. The concentration and the uptake of NO_x⁻ are close to zero. On the other hand, uptake of DIC is sustained. However, carbon fluxes leaving the *E. huxleyi* compartment (cellular mortality and cellular DOC excretion) are now exceeding the DIC uptake leading to the decrease of the *E. huxleyi* carbon biomass. The enhanced *E. huxleyi* mortality caused by viruses increases the fluxes towards the detritus and sediments compartments. The final phase is globally characterised by an increase of the DOC pool. However, the development of the microbial loop is limited by the lack of nitrogen in the ecosystem: bacteria compete with *E. huxleyi* for inorganic nitrogen during this third phase. The total flux of carbon that goes from the *E. huxleyi* compartment to detritic matter and sediment exceeds 22.07 mmol C m⁻³ day⁻¹ in which 6.76 mmol C m⁻³ day⁻¹ (31%) accounts for inorganic carbon and 14.90 + 0.41 mmol C m⁻³ day⁻¹ (69%) for organic carbon.

4. Conclusions

Experimental blooms of *E. huxleyi* induced in mesocosms and related biogeochemical processes were studied using a mechanistic model describing carbon, nitrogen and phosphorus cycling. The model involves a refined representation of biogeochemical processes associated to *E. huxleyi* dynamics including primary production, calcification, cellular DOC excretion, viral lyses and TEP_C formation. The large data-set collected during the experiment constitutes an ideal and unique framework to derive and test the mathematical formulations of the above-mentioned processes. The variability of the cellular C:N ratio governs the dynamics of most of these processes and this stresses the necessity of using an unbalanced growth model in carbon and nitrogen for describing *E. huxleyi* dynamics. Since it appears that calcification starts at the same time as the exhaustion of inorganic nutrients in the mesocosm, a new formulation of calcification as a function of primary production and modulated by the C:N ratio is proposed. This formulation has been found to give a better representation of the observed calcification rates, TA and DIC drawdowns compared to past formulations which were usually based on the biomass or on solely primary production. A correct representation of TEP_C formation has been found tightly dependent on an accurate representation of the cellular DOC excretion by *E. huxleyi*. This last process is also conditioned by the variability of the

cellular C:N ratio. The model succeeds in considering the interaction between *E. huxleyi* cells and pathogen viruses as the most probable cause of an enhanced mortality responsible of the termination of blooms in a confined environment.

The changes in carbon and nitrogen budgets highlighted three phases in the bloom dynamic reflecting the evolution of the cellular C:N ratio and the interaction between hosts and viruses.

The application of the model to the simulation of bloom in real conditions will of course require some adaptations (e.g. impact of zooplankton grazing on the bloom termination, aggregation mechanism, competition with other phytoplankton species, and viral attack). A particular aspect of the model specifically related to the confined environment is the interaction between *E. huxleyi* and viruses. Little information is available concerning the implication of viruses relative to blooms termination in open oceanic conditions. The lower cellular abundance prevailing in open conditions ($1 \text{ to } 8 \cdot 10^6 \text{ cells L}^{-1}$, as reviewed by Harlay et al., 2010), in contrast to mesocosms (up to $60 \cdot 10^6 \text{ cells L}^{-1}$, Fig. 2), may lead to reconsider the explicit representation of the enhanced cellular mortality due to viral lysis. Anyway, this present model can be a good starting tool for applications in open conditions because it contains a well calibrated mechanistic representation of processes associated to *E. huxleyi* development and DIC dynamics. We also plan to test the present model for simulating the mesocosms observations (Bergern, 2001) obtained in high and low $p\text{CO}_2$ conditions in order to appraise, from the model and data analysis, which eventual processes need a reparameterization.

Acknowledgments

The authors are grateful to Jean Pierre Gattuso for providing PAR data during the Bergen experiment and to Anja Engel for her contribution to this work. All the scientists involved in the Pelagic Ecosystem CO_2 Enrichment Study (PeECE) 2001 mesocosm experiment are gratefully acknowledged for providing the data used in the present work. This research was supported by the Belgian Foundation for Scientific research (F.R.S.-FNRS), the EU IP SESAME (contract no. 036949-2), the PEACE project (contract no. SD/CS/03A) financed by the Belgian Federal Science Policy and the EU IP CARBOOCEAN (GOCE-511176). The authors thank the two anonymous reviewers for their comments on the manuscript. M.G., A.V.B. and B.D. are research associates at the F.R.S.-FNRS. This is the MARE publication n° 202 and the NIOO publication n° 4919.

Appendix A. Mathematical formulation of the model

Table 2

List of biogeochemical state variables, description, and units.

State variables	Description	Units
$Eh_{[C,N]}$	<i>Emiliania huxleyi</i> carbon and nitrogen biomass	mmol C,N m^{-3}
$Bact_N$	Heterotrophic bacteria nitrogen biomass	mmol N m^{-3}
Eh_V	Viral density	part m^{-3}
$PCHO$	Polysaccharides TEP precursors	mmol C m^{-3}
TEP_C	TEP	mmol C m^{-3}
NO_x	Nitrate	mmol N m^{-3}
NH_x	Ammonium	mmol N m^{-3}
PO_4	Phosphate	mmol P m^{-3}
DIC	Dissolved inorganic carbon	mmol C m^{-3}
DO	Dissolved oxygen	mmol O_2 m^{-3}
TA	Total alkalinity	mmol m^{-3}
DOC_L, DOC_{SL}	Labile and semilabile dissolved organic carbon	mmol C m^{-3}
DON_L, DON_{SL}	Labile and semilabile dissolved organic nitrogen	mmol C m^{-3}
DOP_L, DOP_{SL}	Labile and semilabile dissolved organic phosphorus	mmol C m^{-3}
Eh_{calc}	Attached calcite on <i>Emiliania huxleyi</i> cells	mmol C m^{-3}
De_{calc}	Free calcite	mmol C m^{-3}
$De_{[C,N,P]}$	Carbon, nitrogen, phosphorus organic detritus	mmol m^{-3}

Table 3
List of ordinary variables.

Variables	Description	Units
T	Temperature	Celsius degree
S	Salinity	
Q_T	Temperature modulating factor	
μ_C	<i>E. huxleyi</i> DIC uptake	mmol $\text{m}^{-3} \text{h}^{-1}$
$Chla$	Chlorophyll a	mg m^{-3}
Eh_P	<i>E. huxleyi</i> phosphorus biomass	mmol m^{-3}
ρ_{Eh}	<i>E. huxleyi</i> respiration	mmol $\text{m}^{-3} \text{h}^{-1}$
NC	<i>E. huxleyi</i> N:C ratio	mol mol^{-1}
λ	Mesocosm half depth PAR	$\mu\text{mol m}^{-2} \text{h}^{-1}$
μ_{NO_x}	<i>E. huxleyi</i> NO_x uptake	mmol $\text{m}^{-3} \text{h}^{-1}$
μ_{NH_x}	<i>E. huxleyi</i> NH_x uptake	mmol $\text{m}^{-3} \text{h}^{-1}$
μ_{PO_4}	<i>E. huxleyi</i> PO_4 uptake	mmol $\text{m}^{-3} \text{h}^{-1}$
μ_{DOP_L}	<i>E. huxleyi</i> DOP_L uptake	mmol $\text{m}^{-3} \text{h}^{-1}$
$\mu_{\text{DOP}_{SL}}$	<i>E. huxleyi</i> DOP_{SL} uptake	mmol $\text{m}^{-3} \text{h}^{-1}$
$\pi_{Eh,[C,N,P]}$	<i>E. huxleyi</i> DOM passive leakage	mmol $\text{m}^{-3} \text{h}^{-1}$
τ_{calc}	Calcite production	mmol $\text{m}^{-3} \text{h}^{-1}$
Ω_{calc}	Calcite saturation state	–
τ_{detach}	Coccoliths detachment	mmol $\text{m}^{-3} \text{h}^{-1}$
τ_{dissol}	Calcite dissolution	mmol $\text{m}^{-3} \text{h}^{-1}$
τ_{ee}	DOC extra excretion	mmol $\text{m}^{-3} \text{h}^{-1}$
R_{vir}	<i>E. huxleyi</i> viral based mortality rate	h^{-1}
$prox$	<i>E. huxleyi</i> cells – viruses proximity	part m^{-3}
$\eta_{Eh,[C,N,P]}$	<i>E. huxleyi</i> mortality	mmol $\text{m}^{-3} \text{h}^{-1}$
$\eta_{Eh_{calc}}$	<i>E. huxleyi</i> mortality based calcite losses	mmol $\text{m}^{-3} \text{h}^{-1}$
$\sigma_{Eh,[C,N,P]}$	<i>E. huxleyi</i> sedimentation	mmol $\text{m}^{-3} \text{h}^{-1}$
$\sigma_{Eh_{calc}}$	Attached calcite sedimentation	mmol $\text{m}^{-3} \text{h}^{-1}$
$\sigma_{det_{calc}}$	Free calcite sedimentation	mmol $\text{m}^{-3} \text{h}^{-1}$
σ_{TEP}	TEP sedimentation	mmol $\text{m}^{-3} \text{h}^{-1}$
$\sigma_{det_{[C,N,P]}}$	Detritus sedimentation	mmol $\text{m}^{-3} \text{h}^{-1}$
$\delta_{det_{[C,N,P]}}$	Decayed detritus	mmol $\text{m}^{-3} \text{h}^{-1}$
δ_{NH_x}	Nitrification	mmol $\text{m}^{-3} \text{h}^{-1}$
$Bact_C$	Bacterial carbon biomass	mmol m^{-3}
$Bact_P$	Bacterial phosphorus biomass	mmol m^{-3}
$\nu_{\text{DOM}_{[C,N,P]}}$	Potential bacteria DOM_L uptake	mmol $\text{m}^{-3} \text{h}^{-1}$
ν_{NH_x}	Potential bacterial NH_x uptake	mmol $\text{m}^{-3} \text{h}^{-1}$
ν_{PO_4}	Potential bacterial PO_4 uptake	mmol $\text{m}^{-3} \text{h}^{-1}$
$\epsilon_{\text{DOM}_{[C,N,P]}}$	Effective bacterial DOM_L uptake	mmol $\text{m}^{-3} \text{h}^{-1}$
ϵ_{NH_x}	Effective bacterial NH_x uptake or excretion	mmol $\text{m}^{-3} \text{h}^{-1}$
ϵ_{PO_4}	Effective bacterial PO_4 uptake or excretion	mmol $\text{m}^{-3} \text{h}^{-1}$
ρ_{bact}	Bacterial respiration	mmol $\text{m}^{-3} \text{h}^{-1}$
θ_{bact}	Bacterial nitrogen biomass growth	mmol $\text{m}^{-3} \text{h}^{-1}$
$\eta_{bact,[C,N,P]}$	Bacterial mortality	mmol $\text{m}^{-3} \text{h}^{-1}$
$\delta_{\text{DOM}_{[C,N,P]}}$	DOM_{SL} hydrolysis	mmol $\text{m}^{-3} \text{h}^{-1}$
δ_{CO_2}	CO_2 air–water interface diffusion	mmol $\text{m}^{-3} \text{h}^{-1}$
δ_{O_2}	O_2 air–water interface diffusion	mmol $\text{m}^{-3} \text{h}^{-1}$

Table 4

The biogeochemical model state equations.

$$\frac{dEh_C}{dt} = \mu_C - \rho_{Eh} - \pi_{Eh_C} - \eta_{Eh_C} - \sigma_{Eh_C} \quad (1)$$

$$\frac{dEh_N}{dt} = \mu_{\text{NO}_x} + \mu_{\text{NH}_x} - \pi_{Eh_N} - \eta_{Eh_N} - \sigma_{Eh_N} \quad (2)$$

$$\frac{dBact_N}{dt} = \theta_{bact} - \eta_{bact_N} \quad (3)$$

$$\frac{dEh_V}{dt} = (\eta_{vir} V_b Eh_C) - (Eh_V V_d Q_T) \quad (4)$$

$$\frac{dPCHO}{dt} = \tau_{ee} (1 - L_{\tau_{ee}}) - (\alpha_{PCHO} PCHO PCHO) - (\beta_{PCHO} PCHO TEP_C) \quad (5)$$

$$\frac{dTEP_C}{dt} = (\alpha_{PCHO} PCHO PCHO) + (\beta_{PCHO} PCHO TEP_C) - \sigma_{TEP} \quad (6)$$

$$\frac{d\text{NO}_x}{dt} = \delta_{\text{NH}_x} - \mu_{\text{NO}_x} \quad (7)$$

$$\frac{d\text{NH}_x}{dt} = \epsilon_{\text{NH}_x} - \mu_{\text{NH}_x} - \delta_{\text{NH}_x} \quad (8)$$

Table 4 (continued)

$$\frac{dPO_4}{dt} = \varepsilon_{PO_4} - \mu_{PO_4} \quad (9)$$

$$\frac{dDIC}{dt} = \rho_{Eh} - \mu_C - \tau_{calc} + \tau_{dissol} - \tau_{ee} + \rho_{bact} + \delta_{CO_2} \quad (10)$$

$$\frac{dDO}{dt} = R_{ON} (\mu_{NO_x} - \delta_{NH_x}) + R_{OC} (\mu_C - \rho_{Eh} + \tau_{ee} - \rho_{bact}) + \delta_{O_2} \quad (11)$$

$$\frac{dT_A}{dt} = 2(\tau_{dissol} - \tau_{calc}) \quad (12)$$

$$\begin{aligned} \frac{dDOC_L}{dt} = & \pi_{Eh_C} + \tau_{ee} L_{\tau_{ee}} + \delta_{DOM_C} + \eta_{Eh_C} D_{\eta_{Eh_C}} P_{sll}(1-P_{ref}) \\ & + \delta_{det_C} P_{sll}(1-P_{ref}) - \nu_{DOM_C} + \eta_{bact_C} F_{bd} F_{bl}(1-P_{ref}) \end{aligned} \quad (13)$$

$$\begin{aligned} \frac{dDOC_{SL}}{dt} = & \eta_{Eh_C} D_{\eta_{Eh_C}} (1-P_{sll})(1-P_{ref}) + \delta_{det_C} (1-P_{sll})(1-P_{ref}) \\ & + \eta_{bact_C} F_{bd} (1-F_{bl})(1-P_{ref}) - \delta_{DOM_C} \end{aligned} \quad (14)$$

$$\begin{aligned} \frac{dDON_L}{dt} = & \pi_{Eh_N} + \delta_{DOM_N} + \eta_{Eh_N} D_{\eta_{Eh_N}} P_{sll}(1-P_{ref}) \\ & + \delta_{det_N} P_{sll}(1-P_{ref}) - \nu_{DOM_N} + \eta_{bact_N} F_{bd} F_{bl}(1-P_{ref}) \end{aligned} \quad (15)$$

$$\begin{aligned} \frac{dDON_{SL}}{dt} = & \eta_{Eh_N} D_{\eta_{Eh_N}} (1-P_{sll})(1-P_{ref}) + \delta_{det_N} (1-P_{sll})(1-P_{ref}) \\ & + \eta_{bact_N} F_{bd} (1-F_{bl})(1-P_{ref}) - \delta_{DOM_N} \end{aligned} \quad (16)$$

$$\begin{aligned} \frac{dDOP_L}{dt} = & \pi_{Eh_P} + \delta_{DOP_P} + \eta_{Eh_P} D_{\eta_{Eh_P}} P_{sll}(1-P_{ref}) - \mu_{DOP_L} \\ & + \delta_{det_P} P_{sll}(1-P_{ref}) - \nu_{DOP_P} + \eta_{bact_P} F_{bd} F_{bl}(1-P_{ref}) \end{aligned} \quad (17)$$

$$\begin{aligned} \frac{dDOP_{SL}}{dt} = & \eta_{Eh_P} D_{\eta_{Eh_P}} (1-P_{sll})(1-P_{ref}) + \delta_{det_P} (1-P_{sll})(1-P_{ref}) \\ & + \eta_{bact_P} F_{bd} (1-F_{bl})(1-P_{ref}) - \delta_{DOP_P} - \mu_{DOP_{SL}} \end{aligned} \quad (18)$$

$$\frac{dEh_{calc}}{dt} = \tau_{calc} - \tau_{detach} - \eta_{Eh_{calc}} - \sigma_{Eh_{calc}} \quad (19)$$

$$\frac{dDet_{calc}}{dt} = \tau_{detach} - \tau_{dissol} + \eta_{Eh_{calc}} - \sigma_{Det_{calc}} \quad (20)$$

$$\frac{dDet_{(C,N,P)}}{dt} = \eta_{Eh_{(C,N,P)}} (1 - D_{\eta_{Eh}}) - \sigma_{det_{(C,N,P)}} - \delta_{det_{(C,N,P)}} + \eta_{bact_{(C,N,P)}} (1 - F_{bd}) \quad (21)$$

Table 5

Mathematical formulation of biogeochemical fluxes.

$$Q_T = Q_{10^{\frac{T-20}{10} \text{Eh.Bact.calc.nit}}} \quad (22)$$

$$Chl_a = NC_{min} \left(NChl_{min} + \left(NChl_{max} - NChl_{min} \right) \frac{NC - NC_{min}}{NC_{max} - NC_{min}} \right) Eh_C \quad (23)$$

$$Eh_P = Eh_N PN \quad (24)$$

Phytoplankton nutrients uptake

$$\mu_C = R_{\mu_C} \frac{\lambda}{\lambda + K_{\lambda} DIC + K_{DIC}} \left(1 - \frac{NC_{min}}{NC} \right) Eh_C Q_{T_{Eh}} \quad (25)$$

$$\rho_{Eh} = R_{\rho_{Eh}} Eh_C + F_{\rho_{Eh}} \mu_C \quad (26)$$

$$pot\mu_{NO_x} = R_{\mu_{NO_x}} \frac{NO_x}{NO_x + K_{NO_x}} \left(1 - \frac{NH_x}{NH_x + K_{NH_x}} \right) \left(1 - \frac{NC}{NC_{max}} \right) Eh_C Q_{T_{Eh}} \quad (27)$$

Table 5 (continued)

$$pot\mu_{NH_x} = R_{\mu_{NH_x}} \frac{NH_x}{NH_x + K_{NH_x}} \left(1 - \frac{NC}{NC_{max}} \right) Eh_C Q_{T_{Eh}} \quad (28)$$

$$pot\mu_{PO_4} = R_{\mu_{PO_4}} \frac{PO_4}{PO_4 + K_{PO_4}} Eh_C Q_{T_{Eh}} \quad (29)$$

$$\begin{aligned} pot\mu_{DOP_{L,SL}} = & R_{\mu_{DOP}} \frac{DOP_L + DOP_{SL}}{DOP_L + DOP_{SL} + K_{DOP}} \left(1 - \frac{PO_4}{PO_4 + K_{PO_4}} \right) \frac{DOP_{(L,SL)}}{DOP_L + DOP_{SL}} Eh_C Q_{T_{Eh}} \\ \text{For } (pot\mu_{NO_x} + pot\mu_{NH_x}) < & \frac{(pot\mu_{PO_4} + pot\mu_{DOP_L} + pot\mu_{DOP_{SL}})}{PN} \end{aligned} \quad (30)$$

$$\mu_{PO_4} = (pot\mu_{NO_x} + pot\mu_{NH_x}) PN \frac{pot\mu_{PO_4}}{pot\mu_{PO_4} + pot\mu_{DOP_L} + pot\mu_{DOP_{SL}}} \quad (31)$$

$$\mu_{DOP_{L,SL}} = (pot\mu_{NO_x} + pot\mu_{NH_x}) PN \frac{pot\mu_{DOP_{L,SL}}}{pot\mu_{PO_4} + pot\mu_{DOP_L} + pot\mu_{DOP_{SL}}} \quad (32)$$

$$\text{For } (pot\mu_{NO_x} + pot\mu_{NH_x}) > \frac{(pot\mu_{PO_4} + pot\mu_{DOP_L} + pot\mu_{DOP_{SL}})}{PN}$$

$$\mu_{NO_x} = \frac{pot\mu_{PO_4} + pot\mu_{DOP_L} + pot\mu_{DOP_{SL}}}{PN} \frac{pot\mu_{NO_x}}{pot\mu_{NO_x} + pot\mu_{NH_x}} \quad (33)$$

$$\mu_{NH_x} = \frac{pot\mu_{PO_4} + pot\mu_{DOP_L} + pot\mu_{DOP_{SL}}}{PN} \frac{pot\mu_{NH_x}}{pot\mu_{NO_x} + pot\mu_{NH_x}} \quad (34)$$

Phytoplankton passive leakage and extra – excretion

$$\pi_{Eh_C} = F_{\pi} \mu_C \quad (35)$$

$$\pi_{Eh_N} = F_{\pi} \max[0; (\mu_{NO_x} + \mu_{NH_x})] \quad (36)$$

$$\pi_{Eh_P} = \pi_{Eh_N} PN \quad (37)$$

$$\tau_{ee} = \gamma_{ee} \frac{\lambda}{\lambda + K_{\lambda} DIC + K_{DIC}} \tau_{calc} Q_{T_{Eh}} \quad (38)$$

Phytoplankton calcification, coccoliths detachment and calcite dissolution

$$\tau_{calc} = R_{calc} Eh_C + F_{C_{calc}} \max[0; \mu_C - \rho_{Eh}] \max \left[0; 1 - \frac{NC}{NC_{max}} \right] \quad (39)$$

$$\tau_{detach} = R_{det} Eh_{calc} + \max \left[0; R_{det_{max}} \left(Eh_{calc} - CC_{max} CC_c \frac{Eh_C}{Eh_{C_{cont}}} \right) \right] \quad (40)$$

$$\tau_{dissol} = R_{diss} Det_{calc} (1 - \Omega_{calc}^{\theta}) Q_{T_{calc}} \quad (41)$$

$$\Omega_{calc} = \frac{0.01028 \frac{S}{35} CO_3}{K_{calcite} 1e6} \quad (42)$$

Virus dynamics

$$prox = \left(Eh_V \frac{Eh_C}{Eh_{C_{cont}}} \right)^{0.5} \quad (43)$$

$$R_{vir} = \eta_{vir_{max}} \left(\tanh \left[\sigma \left(\frac{prox}{th_{EhV}} - 1 \right) \right] - \tanh[-\sigma] \right) \left(1 - \tanh[-\sigma] \right)^{-1} \quad (44)$$

Phytoplankton mortality

$$\eta_{Eh_{(C,N)}} = Eh_{(C,N)} (Q_{T_{Eh}} R_{\eta} + R_{\eta_{vir}}) \quad (45)$$

$$\eta_{Eh_P} = \eta_{Eh_N} PN \quad (46)$$

Table 5 (continued)

$$\eta_{Eh_{calc}} = Eh_{calc} (Q_{T_{Eh}} R_{\eta} + R_{\eta_{vir}}) \quad (47)$$

Phytoplankton, freecalcite, TEP and detritus sedimentation

$$\sigma_{Eh_{[C,N,P]}} = Eh_{[C,N,P]} \frac{Eh_{ss}}{depth} \quad (48)$$

$$\sigma_{det_{calc}} = Det_{calc} \frac{Det_{calc_{ss}}}{depth} \quad (49)$$

$$\sigma_{TEP} = TEP_C \frac{TEP_{C_{ss}}}{depth} \quad (50)$$

$$\sigma_{det_{[C,N,P]}} = Det_{[C,N,P]} \frac{Det_{ss}}{depth} \quad (51)$$

Regeneration and microbial loop

$$\delta_{det_{[C,N,P]}} = R_{\delta_{[C,N,P]}} Q_{T_{Eh}} Det_{[C,N,P]} \quad (52)$$

$$\delta_{NH_x} = R_{nit} \frac{DO}{DO + K_{DO}} Q_{T_{nit}} NH_x \quad (53)$$

$$Bact_C = \frac{Bact_N}{NC_{bact}} \quad (54)$$

$$Bact_P = Bact_N PN_{bact} \quad (55)$$

$$v_{DOM_c} = R_{v_c} Bact_c \frac{DOC_L}{DOC_L + K_{DOC_L}} Q_{T_{bact}} \quad (56)$$

$$v_{DOM_N} = v_{DOM_c} \frac{DON_L}{DOC_L} \quad (57)$$

$$v_{DOM_P} = v_{DOM_c} \frac{DOP_L}{DOC_L} \quad (58)$$

$$\rho_{bact} = v_{DOM_c} (1 - \varepsilon) \quad (59)$$

$$v_{NH_x} = R_{v_{NH_x}} Bact_N \frac{NH_x}{NH_x + K_{bact_{NH_x}}} Q_{T_{bact}} \quad (60)$$

$$v_{PO_4} = R_{v_{PO_4}} Bact_P \frac{PO_4}{PO_4 + K_{bact_{PO_4}}} Q_{T_{bact}} \quad (61)$$

$$\delta_{DOM_{[C,N,P]}} = R_{\delta_{bact}} Bact_c \frac{DOM_{[C,N,P]}}{DOM_{[C,N,P]} + K_{\delta_{DOM_{[C,N,P]}}}} \quad (62)$$

$$\eta_{bact_{[C,N,P]}} = R_{\eta_{bact}} Bact_{[C,N,P]} Q_{T_{bact}} \quad (63)$$

Table 6 (continued)

Par.	Units	Value	Description	Ref.
$NChl_{min}$	mg mol ⁻¹	0.15	Ehux. min. chla: N ratio	(2)
$NChl_{max}$	mg mol ⁻¹	1.2	Ehux. max. chla:N ratio	(2)
$R_{P_{Eh}}$	h ⁻¹	$3.0 \cdot 10^{-3}$	Ehux. basal respiration rate	Adapt. from (2)
$F_{P_{Eh}}$	–	0.1	Fract. of production that is respired	(2)
K_{NO_x}	mmol m ⁻³	1.5	NO _x half-sat.	(2)
K_{NH_x}	mmol m ⁻³	$1.0 \cdot 10^{-2}$	NH _x half-sat. inhibiting NO _x	(c)
$R_{H_{NO_x}}$	mol mol ⁻¹ h ⁻¹	0.2	Ehux. NO _x uptake rate	(c)
K_{NH_x}	mmol m ⁻³	0.1	NH _x half-sat.	(2)
$R_{P_{NH_x}}$	mol mol ⁻¹ h ⁻¹	$5.0 \cdot 10^{-2}$	Ehux. NH _x uptake rate	(2)
K_{PO_4}	mmol m ⁻³	$5.0 \cdot 10^{-2}$	PO ₄ half-sat.	(c)
$K_{IP_{O_4}}$	mmol m ⁻³	0.5	PO ₄ half-sat. inhibiting DOP	(c)
$R_{P_{PO_4}}$	mol mol ⁻¹ h ⁻¹	$5.0 \cdot 10^{-2}$	Ehux. PO ₄ uptake rate	(c)
K_{DOP}	mmol m ⁻³	$1.5 \cdot 10^{-2}$	DOP half-sat.	(c)
R_{DOP}	mol mol ⁻¹ h ⁻¹	$1.0 \cdot 10^{-2}$	Ehux. DOP uptake rate	(c)
F_{π}	–	$2.0 \cdot 10^{-2}$	Ehux. passive leakage	(3)
R_{calc}	h ⁻¹	$1.0 \cdot 10^{-3}$	Ehux. permanent calcif. rate	Adapt. from (7)
$F_{C_{calc}}$	–	1.9	Ehux. calcite : C _{organic} growth ratio	(c)
Eh_{cont}	mmol cell ⁻¹	$2.0 \cdot 10^{-9}$	C _{organic} content of Ehux. cell	Calc. from data
CC_c	mmol ccolith ⁻¹	$1.0 \cdot 10^{-10}$	Calcite content of coccolith	(5)
CC_{max}	ccolith cell ⁻¹	15.0	Max. coccoliths attached on cell surface	(7)
$R_{det_{max}}$	h ⁻¹	0.45	Detachment rate of excess coccoliths	(2)
R_{det}	h ⁻¹	$1.0 \cdot 10^{-3}$	Basal detachment rate of coccoliths	(2)
R_{diss}	h ⁻¹	0.21	Kinetic rate for calcite dissolution	From Keir (1980)
ω	–	4.5	Order of calcite dissolution	From Keir (1980)
$Q_{10_{calc}}$	–	1.3	CaCO ₃ dissolution Q10	From Morse and Arvidson (2002)
γ_{ee}	–	0.8	Fract. of calcif. linked to DOC extra-excr.	Adapt. from (3)
P_{sil}	–	0.13	DOM _L fract. from	(c)
$D_{\eta_{Eh}}$	–	0.34	η_{Eh} and η_{Det} DOM fract. of Ehux. mortality	(1)
P_{ref}	–	0.5	Part. DOM _{refract} and DOM _{non-refract}}	(c)
$L_{\tau_{ee}}$	–	0.1	Fract. of DOM _L in DOC extra excretion	(8)
α_{PCHO}	–	$3.12 \cdot 10^{-5}$	Coagulation coef. of PCHO	(8)
β_{PCHO}	–	$1.07 \cdot 10^{-3}$	Adsorption coef. between PCHO and TEP _C	(8)
$\eta_{vir_{max}}$	h ⁻¹	$2.0 \cdot 10^{-2}$	Max. mortality rate by viral lysis	(c)
th_{EhV}	part m ⁻³	$0.5 \cdot 10^{12}$	Threshold virus-cells proximity	(c)
σ	–	2.0	Slope characterising viral mortality rate	(c)
V_d	h ⁻¹	$1.55 \cdot 10^{-2}$	Virus degeneracy rate	(c)
V_b	part mmol ⁻¹	$5.5 \cdot 10^{11}$	Viral spread-out coef.	From Jacquet et al. (2002) (c)
R_{η}	h ⁻¹	$3.0 \cdot 10^{-3}$	Non-viral Ehux. mortality rate	(c)
$Det_{calc_{ss}}$	m h ⁻¹	$2.0 \cdot 10^{-2}$	Calcite sinking speed	(5)
Eh_{ss}	m h ⁻¹	$1.5 \cdot 10^{-2}$	Ehux. sinking speed	(5)
Det_{ss}	m h ⁻¹	$4.0 \cdot 10^{-2}$	Detritus sinking speed	Calc. from data
$TEP_{C_{ss}}$	m h ⁻¹	$2.0 \cdot 10^{-3}$	TEP _C sinking speed	Calc. from data
depth	m	4.5	Depth of mesocosm water column	From data

Table 6

Parameters values for biological processes.

Par.	Units	Value	Description	Ref.
$Q_{10_{Eh}}$	–	1.5	Ehux. Q10	(6)
R_{μ_c}	h ⁻¹	0.11	Ehux. maximal growth rate	Adapt. from (5)
K_{λ}	μmol m ⁻² s ⁻¹	20	PAR half-sat.	(c)
K_{DIC}	mmol m ⁻³	150	DIC half-sat.	(c)
PN	mol mol ⁻¹	$4.2 \cdot 10^{-2}$	Ehux. P:N ratio	(5)
NC_{min}	mol mol ⁻¹	$5.0 \cdot 10^{-2}$	Ehux. min. N:C ratio	(2)
NC_{max}	mol mol ⁻¹	0.2	Ehux. max. N:C ratio	(2)

Table 6 (continued)

Par.	Units	Value	Description	Ref.
R_{dc}	h^{-1}	$1.88 \cdot 10^{-3}$	Detritus carbon decay rate	(4)
R_{dn}	h^{-1}	$2.29 \cdot 10^{-3}$	Detritus nitrogen decay rate	(4)
R_{dp}	h^{-1}	$2.71 \cdot 10^{-3}$	Detritus phosphorus decay rate	(4)
R_{nit}	h^{-1}	$2.1 \cdot 10^{-3}$	NH_4^+ oxidation rate at 20 dg	(1)
K_{DO}	$mmol\ m^{-3}$	1.0	DO half-saturation for nitrification	(1)
$Q10_{nit}$	–	2.0	Nitrification Q10	(1)
R_{ON}	$mol\ mol^{-1}$	2.0	DO stoichiometry for nitrification	(–)
R_{OC}	$mol\ mol^{-1}$	1.0	DO stoichiometry for biosynthesis	(–)
NC_{bact}	$mol\ mol^{-1}$	0.25	Bact. N:C ratio	(1)
PN_{bact}	$mol\ mol^{-1}$	0.1	Bact. P:N ratio	(1)
$Q10_{Bact}$	–	2.0	Bact. Q10	(1)
$R_{r,c}$	h^{-1}	0.417	Bact. DOC_L uptake rate	(1)
K_{DOC_L}	$mmol\ m^{-3}$	25.0	Bact. DOC_L half-sat.	(1)
K_{bactNH_4}	$mmol\ m^{-3}$	0.5	Bact. NH_4 half-sat.	(1)
K_{bactPO_4}	$mmol\ m^{-3}$	0.01	Bact. PO_4 half-sat.	(1)
F_{bd}	–	0.51	Frac. of bact. mortality consisting of DOM	(1)
F_{bl}	–	0.1	Frac. of bact. $DOM_{non-refrac}$ devoted to DOM_L	(1)
$R_{r,bact}$	h^{-1}	$8.1 \cdot 10^{-3}$	Bact. mortality rate	(1)
ε	–	0.27	Bact. growth efficiency	(1)
R_{bact}	h^{-1}	0.167	Bact. hydrolysis	(1)
$K_{DOMICUP}$	$mmol\ m^{-3}$	417	DOC_{SL} rate Bact. hydrolysis DOC_{SL} half-sat.	(1)

(c) After calibration. References: (1) Anderson and Pondaven (2003), (2) Tyrrell and Taylor (1996), (3) Van Den Meersche et al. (2004), (4) Lancelot et al. (2002), (5) Paasche (2002), (6) Oguz and Merico (2006), (7) Merico et al. (2004), (8) Engel et al. (2004a,b).

References

- Aksnes, D., Egge, J., Rosland, R., Heimdal, B., 1994. Representation of *Emiliania huxleyi* in phytoplankton simulation models. A first approach. *Sarsia* 79, 291–300.
- Anderson, T., Pondaven, P., 2003. Non-Redfield carbon and nitrogen cycling in the Sargasso Sea: pelagic imbalances and export flux. *Deep-Sea Research Part I* 50, 573–591.
- Anderson, L., Sarmiento, J., 1994. Redfield ratios of remineralization determined by nutrient data analysis. *Global Biogeochemical Cycles* 8, 65–80.
- Anderson, T.R., Williams, B., 1998. Modelling the seasonal cycle of dissolved organic carbon at Station E1 in the English Channel. *Estuarine, Coastal and Shelf Science* 46, 93–109.
- Banse, K., 1994. Uptake of inorganic carbon and nitrate by marine plankton and the Redfield ratio. *Global Biogeochemical Cycles* 8, 81–84.
- Brun, R., Kuhni, M., Siegrist, H., Gujer, W., Reichert, P., 2002. Practical identifiability of ASM2D parameters systematic selection and tuning of parameter subsets. *Water Research* 36, 4113–4127.
- Buitenhuis, E., Van Bleijswijk, J., Bakker, D., Veldhuis, M., 1996. Trends in inorganic and organic carbon in a bloom of *Emiliania huxleyi* in the North Sea. *Marine Ecology Progress Series* 143, 271–282.
- Buitenhuis, E., Wal, V.D., De Baar, H., 2001. Blooms of *Emiliania huxleyi* are sinks of atmospheric carbon dioxide: a field and mesocosm study derived simulation. *Global Biogeochemical Cycles* 15 (3), 577–587.
- Delille, B., Harlay, J., Zondervan, I., Jacquet, S., Chou, L., Wollast, R., Bellerby, R., Frankignoulle, M., Vieira Borges, A., Riebesell, U., Gattuso, J.-P., 2005. Response of primary production and calcification to changes of pCO_2 during experimental blooms of the coccolithophorid *Emiliania huxleyi*. *Global Biogeochemical Cycles* 19, GB2023. doi:10.1029/2004GB002318.
- Engel, A., Schartau, M., 1999. Influence of transparent exopolymer particles (TEP) on sinking velocity of *Nitzschia closterium* aggregates. *Marine Ecology Progress Series* 182, 69–76.
- Engel, A., Thoms, S., Riebesell, U., Rochelle-Newall, E., Zondervan, I., 2004a. Polysaccharide aggregation as a potential sink of marine dissolved organic carbon. *Nature* 428, 929–932.
- Engel, A., Delille, B., Jacquet, S., Riebesell, U., Rochelle-Newall, E., Terbrüggen, A., Zondervan, I., 2004b. TEP and DOC production by *Emiliania huxleyi* exposed to different CO_2 concentrations: a mesocosm experiment. *Aquatic Microbial Ecology* 34 (1), 93–104.
- Engel, A., Zondervan, I., Aerts, K., Beaufort, L., Benthien, A., Chou, L., Delille, B., Gattuso, J.-P., Harlay, J., Heemann, C., Hoffmann, L., Jacquet, S., Nejtgaard, J., Pizay, M.-D., Rochelle-Newall, E., Schneider, U., Terbruegggen, A., Riebesell, U., 2005. Testing the direct effect of CO_2 concentration on a bloom of the coccolithophorid *Emiliania huxleyi* in mesocosm experiments. *Limnology and Oceanography* 50 (2), 493–507.

- Engel, A., Schulz, K.G., Riebesell, U., Bellerby, R., Delille, B., Schartau, M., 2008. Effects of CO_2 on particle size distribution and phytoplankton abundance during a mesocosm bloom experiment (PeECE II). *Biogeosciences* 5 (2), 509–521.
- Godoi, R.H.M., et al., 2009. Organic surface coating on coccolithophores—*Emiliania huxleyi*: its determination and implication in the marine carbon cycle. *Microchemical Journal* 91 (2), 266–271.
- Goldman, J.C., Caron, D.A., Dennett, M.R., 1987. Regulation of gross growth efficiency and ammonium regeneration in bacteria by substrate C:N ratio. *Limnology and Oceanography* 32, 1232–1239.
- Harlay, J., Borges, A.V., Van Der Zee, C., Delille, B., Godoi, R.H.M., Schiettecatte, L.-S., Røevros, N., Aerts, K., Lapernat, P.-E., Rebreau, L., Groom, S., Daro, M.-H., Van Grieken, R., Chou, L., 2010. Biogeochemical study of a coccolithophorid bloom in the northern Bay of Biscay (NE Atlantic Ocean) in June 2004. *Progress in Oceanography* 86, 317–336.
- Harlay, J., L. Chou, C. De Bodt, N. Van Oostende, J. Piontek, K. Suykens, A. Engel, K. Sabbe, S. Groom, B. Delille, A.V. Borges (2011) Biogeochemistry and carbon mass balance of a coccolithophore bloom in the northern Bay of Biscay (June 2006), *Deep-Sea Research I*, accepted
- Jacquet, S., Heldal, M., Iglesias-Rodriguez, D., Larsen, A., Wilson, W., Bratbak, G., 2002. Flow cytometric analysis of an emiliana huxleyi bloom terminated by viral infection. *Aquatic Microbial Ecology* 27, 111–124.
- Keir, R.S., 1980. The dissolution kinetics of biogenic calcium carbonates in seawater. *Geochim. Cosmochim. Acta* 44, 241–252.
- Lancelot, C., Stavena, J., Van Eeckhout, D., Beckers, J., Stanev, E., 2002. Modelling the danube influenced north-western continental shelf of the black sea. Ecosystem response to changes in nutrient delivery by danube river after its damming in 1972. *Estuarine, Coastal and Shelf Science* 54, 473–499.
- Mehrbach, C., Culbertson, C., Hawley, J., Pytkowicz, R., 1973. Measurement of the apparent dissociation constants of carbonic acid in seawater at atmospheric pressure. *Limnology and Oceanography* 18, 897–907.
- Merico, A., Tyrrell, T., Lessard, E., Oguz, T., Stabeno, P., Zeeman, S., Whitley, T., 2004. Modelling phytoplankton succession on the bering sea shelf: role of the climate influences and trophic interactions in generating *Emiliania huxleyi* blooms 1997–2000. *Deep-Sea Research Part I*. doi:10.1016/j.dsr.2004.07.003.
- Millero, F., 1995. Thermodynamics of the carbon dioxide system in the oceans. *Geochimica et Cosmochimica Acta* 59 (4), 661–677.
- Morse, J.W., Arvidson, R.S., 2002. Dissolution kinetics of major sedimentary carbonate minerals. *Earth Science Reviews* 58, 51–84.
- Oguz, T., Merico, A., 2006. Factors controlling the summer *Emiliania huxleyi* bloom in the black sea: a modelling study. *Journal of Marine Systems* 59. doi:10.1016/j.jmarsys.2005.08.002:173–188.
- Paasche, E., 2002. Review of the coccolithophorid *Emiliania huxleyi* (prymnesiophyceae), with a particular reference to growth, coccolith formation, and calcification–photosynthesis interactions. *Phycologia* 40 (6), 503–529.
- Passow, U., 2002. Transparent exopolymer particles (TEP) in aquatic environments. *Progress in Oceanography* 55, 287–333.
- Rochelle-Newall, E., Delille, B., et al., 2004. Chromophoric dissolved organic matter in experimental mesocosms maintained under different pCO_2 levels. *Marine Ecology Progress Series* 272, 25–31.
- Schartau, M., Engel, A., Schröter, J., Thoms, S., Völker, C., Wolf-Gladrow, D., 2007. Modelling carbon overconsumption and the formation of extracellular particulate organic carbon. *Biogeosciences* 4, 433–454.
- Shaked, Y., Xu, Y., Leblanc, K., Morel, F., 2006. Zinc availability and alkaline phosphatase activity in *Emiliania huxleyi*: implications for Zn-P co-limitation in the ocean. *Limnology and Oceanography* 51 (1), 299–309.
- Soetaert, K., Herman, P.M.J., Middelburg, J.J., Heip, C., Smith, C.L., Tett, P., Wild-Allen, K., 2001. Numerical modelling of the shelf break ecosystem: reproducing benthic and pelagic measurements. *Deep-Sea Research II* 48, 3141–3177.
- Soetaert, K., deClippele, V., Herman, P., 2002. Femme, a flexible environment for mathematically modelling the environment. *Ecological Modelling* 151, 177–193.
- Soetaert, K., Hofmann, F., Middelburg, J., Meysman, J., Greenwood, J., 2007. The effect of biogeochemical processes on pH. *Marine Chemistry*. doi:10.1016/j.marchem.2006.12.012.
- Suykens, K., Delille, B., Chou, L., De Bodt, C., Harlay, J., Borges, A.V., 2010. Dissolved inorganic carbon dynamics and air–sea carbon dioxide fluxes during coccolithophore blooms in the Northwest European continental margin (northern Bay of Biscay). *Global Biogeochemical Cycles* 24, GB3022. doi:10.1029/2009GB003730.
- Tett, P., Wilson, H., 2000. From biochemical to ecological models of marine phytoplankton. *Journal of Marine Systems* 25, 431–446.
- Toggweiler, J., 1993. Carbon overconsumption. *Nature* 363, 210–211.
- Tyrrell, T., Taylor, A., 1996. A modelling study of *Emiliania huxleyi* in the NE Atlantic. *Journal of Marine Systems* 9, 83–112.
- Van Den Meersche, K., Middelburg, J., Soetaert, K., Van Rijswijk, P., Boschker, H., Heip, C., 2004. Carbon–nitrogen coupling and algal–bacterial interactions during an experimental bloom: modelling a ^{13}C tracer experiment. *Limnology and Oceanography* 49, 862–878.
- Wanninkhof, R., 1992. Relationship between wind speed and gas exchange over the ocean. *Journal of Geophysical Research* 97, 7373–7382.
- Weiss, R.F., 1974. Carbon dioxide in water and seawater: the solubility of a non-ideal gas. *Marine Chemistry* 2, 203–215.
- Xu, Y., Wahlund, T., Feng, L., Shaked, Y., Morel, F., 2006. A novel alkaline phosphatase in the coccolithophore *Emiliania huxleyi* (prymnesiophyceae) and its regulation by phosphorus. *Journal of Phycology* 42 (4), 835–844.
- Zondervan, I., 2007. The effects of light, macronutrients, trace metals and CO_2 on the production of calcium carbonate and organic carbon in coccolithophores. *Deep-Sea Research II* 54, 521–537.